



EDGEWOOD

CHEMICAL BIOLOGICAL CENTER

U.S. ARMY RESEARCH, DEVELOPMENT AND ENGINEERING COMMAND

ECBC-CR-097

BIOLOGICALLY INSPIRED POLYMER MICRO-PATTERNED ADHESIVES

Eugene Cheung
Metin Sitti



CARNEGIE MELLON UNIVERSITY
Pittsburgh, PA 15213

November 2008

Approved for public release;
distribution is unlimited.



20081230006

ABERDEEN PROVING GROUND, MD 21010-5424

Disclaimer

The findings in this report are not to be construed as an official Department of the Army position unless so designated by other authorizing documents.

Blank

PREFACE

The work described in this report was authorized under Contract No. W911NF-07-D-0001. The Task was performed under a Scientific Services Agreement issued by Battelle Chapel Hill Operations, 50101 Governors Drive, Suite 110, Chapel Hill, NC. This work was supported by the Defense Threat Reduction Agency Project No. 8R22GA under the auspices of the U.S. Army Research Office Scientific Services Program administered by Battelle (Delivery Order 0068). This work was started in April 2007 and completed in April 2008.

The use of either trade or manufacturers' names in this report does not constitute an official endorsement of any commercial products. This report may not be cited for purposes of advertisement.

This report has been approved for public release. Registered users should request additional copies from the Defense Technical Information Center; unregistered users should direct such requests to the National Technical Information Service.

Blank

CONTENTS

1.	INTRODUCTION.....	11
1.1	Repeatable Adhesion in Nature.....	11
1.2	Dry Adhesion.....	12
1.3	Wet Adhesion.....	13
2.	MODELING OF BIOLOGICALLY INSPIRED ADHESIVES.....	14
2.1	Dry Adhesion of a Single Fiber.....	14
2.2	Wet Adhesion of a Single Fiber.....	16
2.3	Adhesion of a Fiber Array.....	18
2.4	Summary.....	18
3.	ADHESIVE FABRICATION.....	18
3.1	High Aspect Ratio Microfibers.....	19
3.2	Low Aspect Ratio Micropillars with Oil Coating.....	21
4.	MEASUREMENT SETUPS.....	23
4.1	Sphere-Flat Tensile Adhesion Measurement System.....	23
4.2	Flat-Flat Tensile Adhesion Measurement System.....	24
4.3	Sealing Measurement System.....	25
5.	MODEL VERIFICATION.....	26
5.1	Dry Adhesion.....	26
5.2	Wet Adhesion.....	26
6.	ADDITIONAL SPHERE-FLAT MEASUREMENTS.....	32
6.1	Wet Microfibers on Glass.....	32
6.2	Soft Sphere.....	32
6.3	Rough, Rigid Surface.....	36
6.4	Summary.....	37
7.	FLAT-FLAT TENSILE ADHESION TESTS.....	37
7.1	Initial Tests on Glass.....	38
7.2	Pig Skin Tests.....	39
7.3	Reworked Glass Tests.....	40
7.4	Synthetic Soft Surfaces.....	41
7.5	Wet Substrates.....	42
7.6	Summary.....	43
8.	SEALING TEST RESULTS AND DISCUSSION.....	43

9.	INITIAL FRICTION TESTS.....	44
10.	CONCLUSIONS.....	45
	LITERATURE CITED.....	47

FIGURES

1.	a. Scanning electron microscope image of setae on tarsal pad of beetle <i>Hemisphaerota cyanea</i> 11	11
	b. SEM image showing smooth adhesion pad at end of tibia in aphid <i>Megoura viciae</i> 12	12
2.	Droplets left on glass slide from tarsal footprint of beetle <i>Hemisphaerota cyanea</i> 13	13
3.	Pull-off force for fiber-surface interface 15	15
4.	Diagram showing parameters for capillary adhesion model..... 16	16
5.	Process steps of polymer microfiber fabrication..... 19	19
6.	Scanning electron microscope images of 30 μm diameter fibers, 50 μm edge-to-edge spacing with spatulate tips added 20	20
7.	SEM images of 20 μm diameter fibers, 60 μm edge-to-edge spacing with thin film added..... 21	21
8.	Optical microscope images 23	23
9.	Adhesion characterization system set up for millinewton range measurements..... 24	24
10.	Tensile adhesion measurement setup with passive alignment mechanism 25	25
11.	Sealing measurement setup..... 25	25
12.	Adhesion strength as a function of preload pressure 26	26
13.	Adhesion experiment results as function of silicone oil concentration prior to spinning for 95 μm diameter, 125 μm tall, 71.3 μm edge-to-edge spacing pillars with 1 mN preload, 2 s contact time, and 5 $\mu\text{m}/\text{s}$ retraction speed on a 6 mm glass hemisphere 27	27
14.	Adhesion strength experiment results as function of pillar diameter for 125 μm tall pillars with 5 mN preload, 2 s contact time, and 5 $\mu\text{m}/\text{s}$ retraction speed on a 6 mm glass hemisphere..... 28	28
15.	Estimated normalized volume as function of pillar diameter due to stamping method of liquid application 28	28
16.	Fitted h_0 values used to match the model simulations with experimentally measured wet adhesion values 29	29
17.	Model simulation with initial height h_0 held constant at 0.75 μm 30	30

18.	Model simulation with normalized volume \hat{V} held constant at 0.06.....	31
19.	Adhesion strength experiment results as function of preload for 30 μm diameter, 50 μm edge-to-edge spacing, 125 μm tall polyurethane pillars with 2 s contact time and 5 $\mu\text{m/s}$ retraction speed on a 6 mm glass hemisphere.....	33
20.	Adhesion strength experiment results as function of pillar diameter for 125 μm tall pillars with 5 mN preload, 2 s contact time, and 5 $\mu\text{m/s}$ retraction speed on 6 mm soft polyurethane hemisphere	34
21.	Adhesion strength experiment results as function of preload for 200 μm diameter, 125 μm tall pillars with 2 s contact time and 5 $\mu\text{m/s}$ retraction speed on a 6 mm soft polyurethane hemisphere	34
22.	Adhesion strength experiment results as function of retraction speed for 200 μm diameter, 125 μm tall cylinders with 5 mN preload and 2 s contact time on a 6 mm soft polyurethane hemisphere	35
23.	Adhesion strength experiment results as function of preload for 30 μm diameter, 50 μm edge-to-edge spacing, 125 μm tall polyurethane pillars with 2 s contact time and 5 $\mu\text{m/s}$ retraction speed on a 6 mm soft polyurethane hemisphere.....	36
24.	Adhesion experiment results as function of preload on sanded aluminum substrate for 200 μm diameter pillars, 2 s contact time, and 5 $\mu\text{m/s}$ retraction speed.....	37
25.	Plot of adhesion results vs. preload for (a) bare and (b) spatulate-tipped fiber arrays on flat glass substrate	38
26.	Top view optical microscope images of 50 μm diameter fibers with spatulate tips; (a) high density, (b) medium density, and (c) low density.....	39
27.	Plot of adhesion results vs. preload for various fiber arrays on flat pig skin.....	40
28.	Flat-flat adhesion test results for medium spacing fibers with spatulate tips on glass	40
29.	Flat-flat adhesion test results for medium spacing fibers with spatulate tips on smooth and soft F-15.....	41
30.	Flat-flat adhesion test results for medium spacing fibers with spatulate tips on textured soft F-15 with RMS roughness of 1.39 μm	42
31.	Flat-flat adhesion test results for medium spacing fibers with spatulate tips on glass with thin water layer.....	42
32.	ST-1060 polyurethane molded fiber array, cut into 1 in. diameter annulus, with spatulate tips and encapsulation.....	43

TABLES

1.	Material properties of candidate viscous liquid coatings for beetle foot-hair inspired adhesive secretions.....	22
2.	Sample geometry for experimentally tested polyurethane fibers.....	38
3.	Friction measurements on soft F-15 polyurethane with 1.39 μm RMS roughness with pulling speed of 0.1 mm/s	44

Blank

BIOLOGICALLY INSPIRED POLYMER MICRO-PATTERNED ADHESIVES

1. INTRODUCTION

The U.S. Army Edgewood Chemical Biological Center (ECBC) is investigating novel sealing technologies for respiratory protective masks to address current shortfalls in operational performance due to improper fitting and donning practices. One promising area is biologically inspired dry adhesives. Geckos, spiders, beetles, flies, and many other climbing lizards and insects have a variety of sub-millimeter scale fibers on their feet to robustly and efficiently climb on a wide range of smooth and rough surfaces. These micro/nano structures enable strong, robust, and repeatable adhesion and friction in addition to being self-cleaning of dirt and other contaminants on surfaces. This work aims to investigate the usage of a synthetic version of these fibrillar adhesion mechanisms in improving mask sealing performance.

1.1 Repeatable Adhesion in Nature

As early as Hooke in 1665, Blackwall in 1830, and West in 1862, studies have been conducted on the adhesive structures on the legs of insects.¹ With only their early microscopes, they could describe morphology well but lacked the tools to analyze function. Now armed with devices that can see at length scales only dreamed about in the 19th century, today's scientists and engineers know a great deal more about insect adhesion systems, but there is still much to learn. Tests have shown some insects capable of holding 60 times their body weight for as long as 2 minutes at a time², and yet these insects must also be able to run on the same surface. The mechanism for balancing these two is not yet fully understood. While the exact structure obviously depends on the species, insect legs have a general form. A pair of claws in addition to numerous stalks called setae on a footpad known as the pulvillus can be found at the end of each walking leg.³ In addition to these structures, insects can have specialized adhesion organs on the tibia and tarsus. These can either be covered with more setae or tenent hairs as in flies and beetles (see Figure 1a) or they can be just a smooth pad as in cockroaches, aphids, and ants (see Figure 1b).³



Figure 1a. Scanning electron microscope (SEM) image of setae on tarsal pad of beetle *Hemisphaerota cyanea*. [Scale bar = 100 microns (adapted from Eisner and Aneshansley)].²



Figure 1b. SEM image showing smooth adhesion pad (p) at end of tibia in aphid *Megoura viciae*. [ta = tarsus. ti = tibia. Scale bar = 20 microns (adapted from Lees and Hardie)].⁴

The claws are mainly for locomotion over rough surfaces where the insect can make a mechanical attachment much like a human grabbing onto a knob on a rock face. It has been shown that adhesion to smooth surfaces is not affected by the removal of the insect's claws.⁵

Early biologists suggested many possible explanations for insect adhesion. The two main methods that have been soundly discounted experimentally are electrostatic adhesion and suction.^{5,6} Stork used a Zerostat antistatic gun, which emits ions from a piezoelectric crystal to neutralize electrostatic forces on each leaf beetle, *Chrysolina polita*, in his tests and found no decrease in adhesive force. Dixon et al. performed a similar test with their aphids with the same result. Additionally, the aphids were still able to walk on glass after treading on filter paper moistened with 1% salt solution. No electric potential can be generated between the insect and substrate if they are connected via a dielectric. To test suction as a means of generating adhesion, Stork placed his leaf beetles in a reduced pressure environment. Since the power of suction is dependent on the pressure difference between the suction cup and the surrounding environment, a decrease in adhesive force would be expected. No such decrease was observed, indicating suction is not a cause for insect adhesion. Dixon et al. took a different approach, but with similar results. The suction must be generated by muscle flexure, therefore a muscle relaxant should cause attached aphids to detach if suction were indeed occurring. Administration of carbon dioxide anesthesia did not result in any aphid detachment.

1.2 Dry Adhesion

Molecular, or dry, adhesion is another possible explanation. This type of adhesion is commonly associated with fibrillar surfaces (such as the setae shown in Figure 1a); the toes of a gecko, widely recognized as the classic example of dry adhesion, are covered with hierarchical foot hairs capable of adhesion strengths as high as 100 kPa.⁷ Dry adhesion is hypothesized to result from the relatively weak van der Waals molecular attractive force that is only significant at length scales below a micrometer. Fibrillar surfaces achieve the required intimate contact through the compliance of the long, slender fibers.⁸ Consider a non-uniform substrate with random asperities. When a flat surface is brought into contact, only the asperities make contact with the flat surface. If, however, the flat surface is covered with long, slender

fibers, the fibers in contact with the asperities can locally bend to allow the rest to make contact with the substrate. When summed up over the millions of fibers, the tiny molecular force becomes a macroscopic total force capable of supporting an organism's weight.

Since Autumn's signal paper in 2000 that measured the adhesion of a single gecko seta,⁷ a wealth of research has been published in understanding, modeling, and mimicking fibrillar adhesion. Arzt *et al.* modeled single fiber contact using Johnson, Kendall, and Roberts (JKR) theory, showing that splitting a single contact area into many little contacts that sum to the same area results in greater adhesion.⁹ Contacts mechanics researchers have suggested another method of adhesion enhancement derived from fibrillar surfaces, a theory known as "crack trapping."^{10,11} In this theory, the discrete nature of fibrillar contact prevents crack propagation that would otherwise occur in a continuous contact.

1.3 Wet Adhesion

While most insects have some form of setae, many insects have also been found to secrete some sort of liquid to aid in adhesion.^{1,2,4,6,12-17} In most cases, the evidence was gathered by simply conducting the tests on a glass slide. Once the insects were removed, there remained liquid droplets that could be studied. The liquid, seen in Figure 2, was identified as a light oil at first.^{2,4,6,17} Kosaki and Yamoaka were more specific, stating the liquid consisted of hydrocarbons and true waxes. However, the most recent papers amend these findings a little. One found that the liquid secreted by ants was a base of hydrophobic liquid that contained a volatile, hydrophilic phase.¹ Another suggests that the pad secretion from the locust *Locusta migratoria* is an emulsion of lipidic nano-droplets dispersed in an aqueous, water-soluble liquid.¹⁶

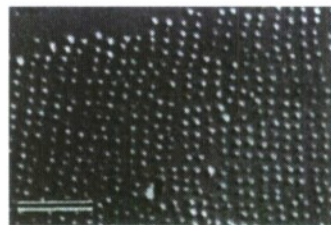


Figure 2. Droplets left on glass slide from tarsal footprint of beetle *Hemisphaerota cyanea*. [Scale bar = 50 microns (adapted from Eisner and Aneshansley)].²

Eisner and Aneshansley reported that for the blue beetle *Hemisphaerota cyanea*, the liquid is released by pores along the base of the setae.² The beetle generates the liquid via the processing of its food source, palmetto plants that are naturally rich in waxes. Gorb found pores at the distal ends of the setae in a fly, suggesting that there was a channel of some sort within each seta through which fluid could flow.¹² Much of the evidence suggests that the liquid is stored just below the surface in most cases, getting released out of porous channels when pressure is applied to the area.

The liquid secretions are thought to cause adhesion through capillary forces, but a complete model has yet to be presented. Many have simplified the problem to a simple liquid bridge with a pressure drop across the interface dictated by the surface tension and shape of the liquid bridge.^{3,4} Lees and Hardie, in their experiments with the aphid *Megoura viciae*, found

that if they approximated the secretion as a light mineral oil and deduced a liquid bridge shape from the volume of the secreted droplets, they obtained an adhesion force two orders of magnitude greater than experimental values. It can be seen that, although surely an overestimate with their approximations, capillary adhesion has enough force to be a viable explanation for insect adhesion on smooth surfaces. Qian and Gao proposed a numerical solution to the liquid bridge shape, showing that their results scale down favorably.¹⁸

2. MODELING OF BIOLOGICALLY INSPIRED ADHESIVES

The first step in the design of biologically inspired microfibrillar adhesives is the development of approximate mathematical models that capture the different types of forces that contribute to adhesion. These models can then be used to gain insight into the performance of fabricated adhesives and suggest possible improvements.

2.1 Dry Adhesion of a Single Fiber

An approximate analytical model for dry fiber adhesion has been developed by combining the basic principles of elastic beam theory, surface interaction forces, and contact mechanics and applying them to high aspect ratio vertical and angled microfibers.¹⁹ First, flat punch theory is used to find the average adhesion strength of a single fiber. Next, beam mechanics is used to find the tensile stresses at the interface during loading. The pull-off force is determined by equating an “average tensile stress” to the average adhesion strength. Finally, the pull-off force is related to fiber deflection through linear elastic beam equations. In reality, the pull-off is a complex process due to the singular stresses and non-linearities at the fiber-surface interface. However, in the model, the criteria for pull-off were derived using the moments, forces, and stresses at the interface through a simplified linear model. This approximate linear model may not lead to the exact solutions, but should describe the general trends in adhesion performance when varying the design parameters.

The fiber geometry is taken as a cylindrical beam with a flat tip which closely approximates the fabricated microstructures discussed in Section 3.1. Assuming the fiber contacts a locally flat surface, the adhesion (P_f) for a circular flat punch and a flat surface interaction is given as

$$P_f = \sqrt{6\pi a^3 K w_f} \quad (1)$$

$$K = \frac{4}{3} \left(\frac{1 - \nu_s^2}{E_s} + \frac{1 - \nu_f^2}{E_f} \right)^{-1} \quad (2)$$

where w_f is the effective work of adhesion, a is the fiber radius, and K is the effective Young's modulus. E_s and E_f are the Young's moduli and ν_s and ν_f are the Poisson's ratios of the surface and the fiber material, respectively.²⁰ Although eq (1) is derived from a rigid punch on an elastic soft surface, it is also a good first order approximation for an elastic punch which is softer than the flat surface²¹ as is the case for some of the polymer microfibers discussed in this work.

Using the pull-off force of a circular flat punch, the average adhesion strength (σ_c) can be determined as

$$\sigma_c = \frac{P_f}{\pi a^2} \quad (3)$$

The pull-off of a single fiber is said to be *flaw insensitive*¹¹ if the pull-off is controlled by the adhesive properties of the interface rather than the crack propagation. This condition is satisfied when the radius of the fiber (a) is less than a critical length $d_c = 6Kw/(\pi\sigma_o^2)$ where σ_o is the intrinsic adhesion strength.²² This is an important condition for strong adhesion because the fiber tip is not guaranteed to be perfectly smooth and flat, and any defects could introduce cracks at the interface.

To determine the pull-off force for the fiber-surface interface, the fiber is modeled as a fixed-guided cylindrical beam as shown in Figure 3a. The fixed boundary condition occurs at the end of the fiber that is affixed to the backing layer and the fiber is assumed not to rotate or move at this end. The other end of the fiber, which is referred to as the tip of the fiber, is adhered to a surface and is assumed to have guided boundary condition, meaning that the fiber tip moves only in the direction normal to the backing layer (n -direction) and the undeformed angle at the tip is maintained (Figure 3b). The moment (M_x) is found from the rotation constraint at the fiber tip as

$$M_x = \frac{P_y L}{2} \quad (4)$$

where L is the length of the fiber. The force exerted on the fiber tip in y -direction (P_y) is related to the resultant force in n -direction through $P_y = P_n \sin\theta$ where θ is the fiber angle. M_x introduces a normal stress at the fiber tip which is compressive for one half of the tip and is tensile for the other half.

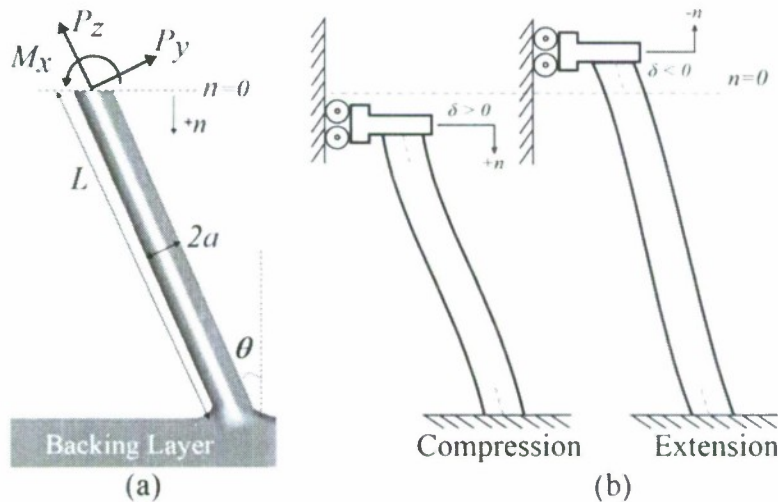


Figure 3. Pull-off force for fiber-surface interface.

(a) Schematic of forces on tip of single fiber.

(b) Illustration of fixed-guided boundary conditions of fiber in contact with locally flat surface during compression and extension (the angle of the fiber at both ends remains fixed while the tip moves only in the n direction).

In addition, the force in z-direction $P_z = P_n \cos \theta$ creates a uniform tensile stress on the entire tip. Thus, the average stress on the half of the fiber tip (σ_{av}) where the moment M_x causes a tensile stress is

$$\sigma_{av} = c \left(\frac{P_n \cos \theta}{\pi a^2} + \frac{8P_n L \sin \theta}{3\pi^2 a^3} \right) \quad (5)$$

where c is the stress transformation factor. Since the tip of the fiber is not perpendicular to the axis of the fiber, the stress needs to be transformed to the tip plane and for this specific case $c = \cos^2 \theta$. For angled fibers, the pull-off force (P_{cf}) is chosen to be the force in the n -direction (P_n) that causes the average tensile stress (σ_{av}) to reach the average adhesion strength (σ_c). Thus by replacing P_n with P_{cf} and σ_{av} with σ_c , eq (5) can be rewritten to obtain the pull-off force (P_{cf}) as

$$P_{cf} = \frac{3\pi^2 a^3 \sigma_c}{(\cos^2 \theta)(3\pi a \cos \theta + 8L \sin \theta)} \quad (6)$$

Note from eqs (3) and (6) that when $\theta = 0^\circ$, $P_{cf} = P_f$ which is the pull-off force for vertical fibers.

2.2 Wet Adhesion of a Single Fiber

An analogous simple model for the description of maximum force during viscous liquid bridge extension (geometry seen in Figure 4) has yet to be reported.

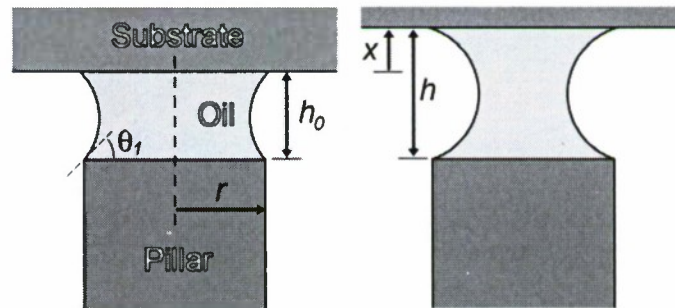


Figure 4. Diagram showing parameters for capillary adhesion model. (The volume of the silicone oil bridge is exaggerated for clarity.)

Qian and Gao proposed a doubly iterative solution to a system of ordinary differential equations arising from the Young-Laplace equation that finds the static shape of the liquid bridge between a flat punch and infinitely flat substrate at a given extension from which the capillary force can be computed.¹⁸ The Young-Laplace equation is given by

$$\Delta P = \gamma \left(\frac{1}{R_1} + \frac{1}{R_2} \right), \quad (7)$$

where ΔP is the pressure drop across the liquid surface, γ is the liquid surface tension, and R_1 and R_2 are the principal radii of curvature of the liquid bridge. Rewriting in terms of the arc length of the liquid profile, s , gives the following system of ordinary differential equations:

$$\begin{aligned}\frac{dr}{ds} &= \cos \varphi \\ \frac{dz}{ds} &= \sin \varphi \\ \frac{d\varphi}{ds} &= \frac{\Delta P}{\gamma} - \frac{\sin \varphi}{r}\end{aligned}\quad (8)$$

where r is the radial coordinate, z is the axial coordinate, and φ is the angle between the local tangent of the liquid profile and the r axis. The profile of the liquid bridge can be solved using this system of equations given the liquid volume, contact angles, and height of the liquid bridge by iteratively guessing values for ΔP and r_0 , the radius of the wetted area on the pillar. The liquid bridge profile and pressure difference can then be used to find the total force on the flat punch using

$$F_{static} = -\pi r^2 \Delta P + 2\pi r \gamma \sin \theta_1 \quad (9)$$

where r is the radius of the wetted area of the flat punch and θ_1 is the contact angle between the flat punch and the liquid.

Qian and Gao showed that the maximum adhesion force occurs at a small liquid bridge height where the liquid approaches more of a thin-film configuration and completely wets the base of the flat punch. As such, a viscous force term can be added to eq (9) that is taken from thin-film lubrication theory. The Stefan equation, which describes the force required for a squeezing flow of liquid between two parallel disks of radius r separated by a distance h , is given by

$$F_{viscous} = \frac{3\pi\mu r^4 \dot{h}}{2h^3} \quad (10)$$

where μ is the dynamic viscosity of the liquid and $\dot{h} = dh/dt$ is the speed at which the plates are moving relative to each other.²³

The final force that may be included in the model is the van der Waals force that is present regardless of any liquid coating. The force between a flat punch of radius r and a flat surface that is a distance h away is given by

$$F_{vdW} = \frac{Ar^2}{6h^3} \quad (11)$$

where A is the Hamaker constant of the materials.²⁴

The sum of the three forces discussed above yields the total adhesion force between a flat punch of radius r and a substrate separated by a liquid thin film:

$$F = -\pi r^2 \Delta P + 2\pi r \gamma \sin \theta_1 + \frac{3\pi \mu r^4 \dot{h}}{2h^3} + \frac{Ar^2}{6h^3} \quad (12)$$

It is important to note that, unlike the dry adhesion model, the wet adhesion force can be greatly affected by the measurement method due to the damping term. Therefore, to compare any experiments with this model the adhesion measurement setup described in Section 4.1 must be included in the calculations. The system dynamics can be simply modeled as a mass (contact probe), spring (sensing element), and damper (liquid bridge) system. The base of the spring, with spring constant k , moves at a defined velocity v , while the base of the damper is fixed. The force of the damper is given by eq (12)(12) This leads to the differential equation

$$m\ddot{x} = k(vt - x) - \left(-\pi r^2 \Delta P + 2\pi r \gamma \sin \theta_1 + \frac{3\pi \mu r^4 \dot{x}}{2(h_0 + x)^3} + \frac{Ar^2}{6(h_0 + x)^3} \right) \quad (13)$$

where x is the height of the glass hemisphere, \dot{x} and \ddot{x} are time derivatives of the height, h_0 is the initial liquid film height, and t is time. ΔP and θ_1 are functions of time solved from the Qian and Gao model. The initial conditions are $x = 0$ and $\dot{x} = 0$, which corresponds to the end of the contact time just as the actuator begins retracting the base of the sensing element away from the adhesive sample. This differential equation is numerically solved using a fourth-order Runge-Kutta technique to predict measured adhesion values.

2.3 Adhesion of a Fiber Array

Determining the adhesion of an array of fibers is not simply the product of the number of fibers in the array and the single fiber adherence. Fiber array adhesion is a function of many parameters such as fiber geometry, fiber spacing, and surface topography of the adhering surface. Knowing the value of these parameters, it is possible to expand the single fiber models from the previous sections to evaluate the adhesive behavior of an array of fibers where each fiber has a deflection which is a function of the surface topography and the relative displacement between the surfaces.

2.4 Summary

The models are implemented in MATLAB and C code to simulate the adhesion of single fiber contacts and fiber arrays. Material properties and fiber geometries are varied to match the experiments conducted. The combined results of simulations and experiments will be used to verify the proposed approximate models and gain some insight into natural fibrillar adhesion mechanisms and synthetic fibrillar adhesive design.

3. ADHESIVE FABRICATION

Two different types of patterned polymer adhesives were fabricated for testing. Small diameter (less than 50 μm), high aspect ratio microfibers were used to verify the dry adhesion model. Tip modifications were also made on these microfibers as these additions have been reported to improve adhesion. Large diameter (up to 340 μm), low aspect ratio micropillars were used for wet adhesion as this model doesn't include length effects.

3.1 High Aspect Ratio Microfibers

Polymer microfiber arrays are fabricated through a micromolding process which duplicates lithographically formed master template structures with a desired fiber material. The master template is produced using a negative photoresist (SU-8 2000; MicroChem, Newton, MA) on a glass wafer substrate. First, a thin layer of SU-8 is spun onto the wafer to provide a thin polymer backing for the microfibers. The layer is baked and uniformly exposed with UV light (Figure 5a) to provide a surface to which the microfibers can firmly anchor. Next, another layer of SU-8 is spun atop the first layer (Figure 5b). The thickness of this layer determines the height of the microfibers. A transparency mask (Output City, Bandon, OR) with circular clear areas of specified diameter in a square packing arrangement is used to pattern the wafer with directional UV light (Figure 5c). Each patch of circles in a certain geometry is a 1-in. square. The unexposed regions are removed by immersion in a developer bath (SU-8 developer; MicroChem, Newton, MA), leaving the desired microfiber array (Figure 5d).

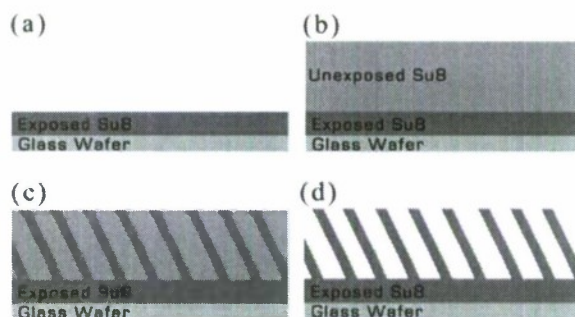


Figure 5. Process steps of polymer microfiber fabrication.

- (a) Thin layer of SU-8 is spun on glass substrate then exposed and cured.
- (b) Thicker layer of SU-8 is spun and it becomes the fibers.
- (c) Thick layer is patterned with UV exposure.
- (d) SU-8 photoresist is developed, leaving desired fiber array.

Since the SU-8 material properties are not ideal for use as a structural material due to its brittleness and weak bond with the backing substrate, it is desirable to create a mold in which to replicate the fibers with a different polymer material. Moreover, molding enables the selection of a wide range of polymer materials as the fiber material, the master template can be used tens or hundreds of times, which increases the fabrication speed and reduces the cost significantly. A compliant mold is fabricated by pouring a liquid silicone rubber (HS II; Dow Corning, Midland, MI) over the wafer and allowing it to cure at room temperature for 24 hr. Once cured, the mold is carefully peeled away from the template wafer resulting in a flexible mold with a negative shape of the SU-8 fibers. This mold is used to vacuum mold liquid polyurethanes or other curable materials (except silicone rubbers which bond to the template rubber material) with the desired physical properties. The thickness of the polymer can be controlled by placing a flat surface over the liquid polyurethane, separated from the compliant mold with a spacer of the desired thickness. Once cured and de-molded, the polyurethane fibers have roughly the same geometry as the original SU-8 fibers. In this work, the polyurethane ST-1060 (BJB Enterprises, Tustin, CA) is chosen for its compliance, durability, and high surface energy.

Spatulate Tips

The tips of gecko setae and most other biological fibrillar attachment mechanisms are comprised of a flat spatula with a larger diameter than the fiber itself. To mimic this in the synthetic adhesive, a thin layer (approximately 10 μm) of uncured polyurethane is spun onto a polystyrene Petri dish. The thickness and diameter of the resulting spatulae are determined by the thickness of this layer. A polymer fiber array is then placed gently onto this layer, with the tips of the fibers dipping into the uncured polymer. The array is then lifted off of the Petri dish, resulting in a small amount of uncured polymer on the tip of each fiber. The tips are flattened into spatula by then placing the fiber array onto a flat surface, tips down, and curing at room temperature for 12 hr. The resulting spatulate tipped fiber array, shown in Figure 6, can then be peeled off the flat surface.

Thin Film

The addition of a thin film is very similar to the spatulate tip fabrication. After dipping in the thin layer of uncured polymer, the microfibers are merely left there to allow the polymer to cure into a thin film. To obtain a truly thin film (Glassmaker et al. reported a 4 μm PDMS film)²⁵ with ST-1060, some slight modifications to the procedure are necessary. Since the uncured polyurethane is more viscous than uncured PDMS, the ST-1060 must be diluted with a volatile solvent similar to what is done with the silicone oil in Section 3.2. It was found that mixing ST-1060 with acetone in a 1:2 ratio by weight successfully diluted the polyurethane to allow a much thinner layer upon spinning. Testing showed that the acetone dilution does not affect the adhesive properties of ST-1060, although the material becomes slightly softer (Young's modulus decreases by approximately 10%). Furthermore, as acetone attacks polystyrene, the diluted polyurethane was spun onto a glass wafer. The adhesion between ST-1060 and glass is high enough that peeling the thin film from the glass wafer typically results in the tearing of the film. To help alleviate this problem, the peeling was performed in water. Although glass and ST-1060 are not hydrophobic, the water seems to prevent the majority of tearing that occurs during peeling. An SEM image of ST-1060 fibers with attached thin film is shown in Figure 7.

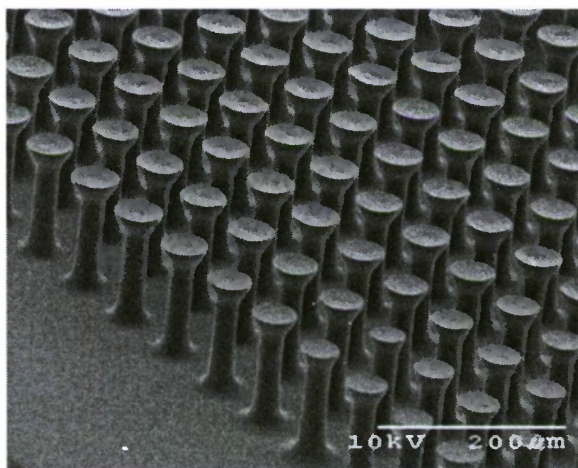


Figure 6. Scanning electron microscope images of 30 μm diameter fibers, 50 μm edge-to-edge spacing with spatulate tips added.

Polymer micropillar arrays are created using the standard technique for fabrication of stamps in soft lithography.²⁶ A master mold is produced by coating a glass or silicon wafer with photoresist (SU-8 2000; MicroChem, Newton, MA). The wafer is then exposed to an ultraviolet light source through a printed transparency mask (PageWorks, Cambridge, MA). The unexposed regions are removed by immersion in a developer bath (SU-8 developer; MicroChem, Newton, MA). Uncured poly(dimethylsiloxane) (PDMS) (Sylgard 184; Dow Corning, Midland, MI) is poured into the master mold, degassed, and cured at 75 °C for 2 hr. PDMS is the chosen polymer for ease of fabrication, handling, and imaging due to its transparency. The micropillars are obtained by mechanically peeling the cured PDMS pillars from the master mold. The height of the patterns is determined by the thickness of the photoresist, and all other geometries are controlled by the shapes on the printed transparency mask. For this study, the micropillars were fabricated as hexagonally packed cylinders 125 μm tall with diameters ranging from 80 to 340 μm. These diameters were chosen because a dry adhesion peak was expected in this range¹⁰ and for their ease of fabrication. The edge-to-edge spacing was set to a multiple of the pillar diameter such that the area fraction remained constant. Each diameter micropillar was fabricated in a square array of area approximately 300 mm² such that all of the required samples could be produced using a single wafer; this reduces any extra uncertainties due to process variations.

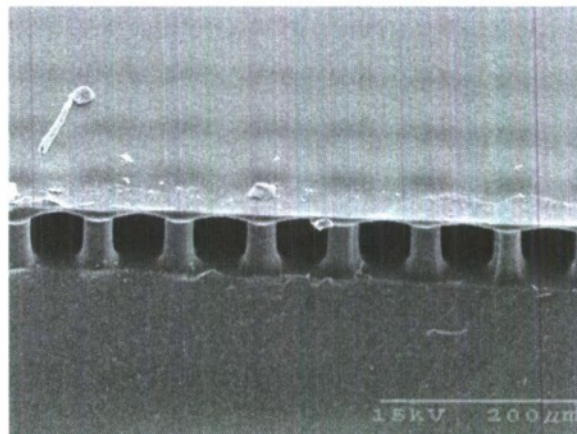


Figure 7. SEM images of 20 μm diameter fibers, 60 μm edge-to-edge spacing with thin film added.

The final step was the application of a liquid layer on the PDMS micropillars. The basic capillary adhesion formula $F=4\pi\gamma R\cos\theta$ for a sphere-plane interface²⁴ indicates the importance of a high surface tension (γ) and low contact angle with the surfaces (θ) where R is the sphere radius. Unfortunately, those liquids that have small contact angles on a wide variety of surfaces, namely waxes or oils, also typically have a low surface tension (roughly 30 mN/m, or 40% that of water). As the range of contact angles has a more pronounced effect on the resulting capillary adhesion, it is more desirable to sacrifice surface tension for a robust, low contact angle. Indeed, the secretions of various insects have been found to be comprised of mainly hydrophobic oils and fatty acids, leading to a liquid with low surface tension and low contact angle.^{1,16}

Additionally, the viscosity of the liquid is believed to play a major role as the natural secretions are many orders of magnitude more viscous than water. Federle *et al.*

estimated the viscosity of the secretions of an ant to be as high as 150 mPa·s, which is about 1500 cSt if the density is assumed to be close to that of water.¹ Table 1 shows the values of these material properties for several candidate synthetic liquids. As in the biological systems, silicone oil was chosen for this study despite its low surface tension due to its low contact angle, biocompatibility (significant for potential biomedical applications), and flexibility in choosing its viscosity (a wide range is readily available from manufacturers). For the majority of tests, a silicone oil much more viscous than the liquid seen in nature was used in an attempt to enhance the capillary adhesion; biological systems suffer from energy limitations that would preclude them from producing and using liquids of extremely high viscosities.

Table 1. Material properties of candidate viscous liquid coatings for beetle foot-hair inspired adhesive secretions. (The contact angles were independently measured with a goniometer. Water is included as a baseline.)

Liquid	Surface Tension (mN/m)	Viscosity (cSt)	Contact Angle (°) on PDMS
Water	72.8	1	105
Hexadecane	27.5	10	40
Silicone Oil	21.5	50—10000	15
Ethylene Glycol	47.7	15.7	90
Glycerol	64.0	1300	100

The liquid application was achieved by quickly stamping the micropillars onto a wafer spin-coated with a layer of silicone oil (200 Fluid; Dow Corning, Midland, MI). When a pure silicone oil with a viscosity of 10,000 cSt was spun at 6000 RPM for 190 s, the resulting liquid layer was approximately 10 μm thick. The silicone oil can be thinned with xylene (Fisher Scientific, Pittsburgh, PA) prior to spinning; the solvent evaporates quickly when the solution is spun, leaving a thinner liquid layer of the original viscosity.

Since this is a stochastic process, the actual amount of silicone oil transferred to the micropillars is estimated using both profile and inverted view optical microscope images taken just prior to the adhesion experiments. The oil drops are always approximated as sections of a sphere, whose volume is given by

$$V = \pi h^2 R - \frac{1}{3} \pi h^3 \quad (14)$$

where h is the height of the section and R is the radius of the sphere. When the oil drop completely covers the top of the pillar as in Figure 8a, eq (14) can be used to calculate the oil drop volume with

$$R = \frac{1}{2h} (r_p^2 + h^2) \quad (15)$$

The radius of the pillar r_p and oil drop height h are measured from the profile view image. When the oil drop does not cover the top of the pillar as seen in Figure 8b, eq (14) can be used to calculate the oil drop volume with

$$R = \frac{r_d}{\sin \theta} \quad (16)$$

$$h = R(1 - \cos \theta) \quad (17)$$

where θ is the contact angle and the radius of the oil drop r_d is measured from the top view microscope image.

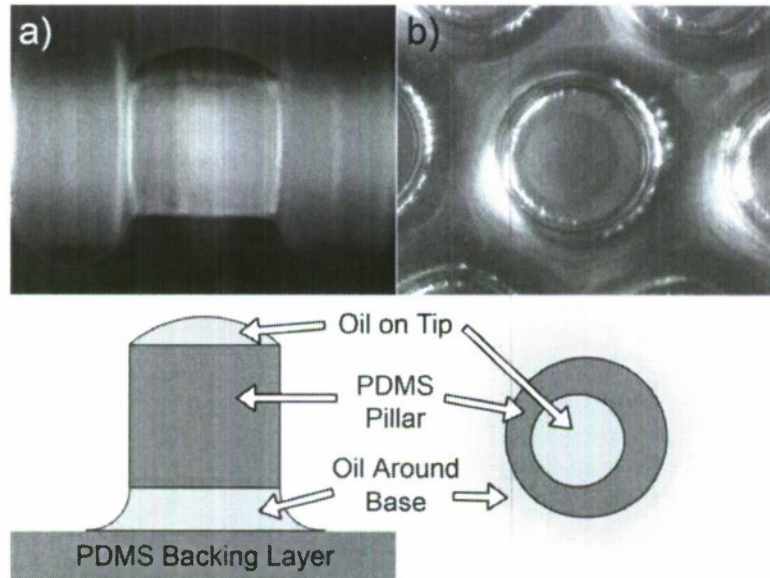


Figure 8. Optical microscope images.
 (a) Profile view of 95 μm diameter PDMS micropillar.
 (b) Top view of 200 μm micropillar. Both have silicone oil coating.

4. MEASUREMENT SETUPS

A series of different measurement setups were used during this research. The first was a tensile adhesion measurement system for sphere-flat (substrate-adhesive) contact that was used in model verification. The second was another tensile adhesion measurement system for flat-flat contact to capture macro-scale effects. The final was a vacuum-assisted sealing measurement system to characterize the sealing capabilities of the adhesives on various substrates.

4.1 Sphere-Flat Tensile Adhesion Measurement System

The sphere-flat tensile adhesion measurement system was built on an inverted optical microscope (Eclipse TE200; Nikon, Melville, NY) to enable real-time imaging of the real micropillar and liquid contact area and the liquid bridge dynamics. This system consists of an automated high precision linear actuator (MFA-CC; Newport, Irvine, CA) that controls a sensing element. For millinewton range adhesion measurements, this element was a 25 g load cell (GSO-25; Transducer Techniques, Temecula, CA) with a 6 or 12 mm diameter hemisphere attached to the load point, seen in Figure 9. A hemisphere was used to eliminate any

uncertainties due to alignment errors as well as to enable the isolation of single pillar contacts for the large low aspect ratio micropillars. For sub-millinewton range adhesion measurements, the sensing element was a thin glass cantilever beam cut from a #1 glass coverslip with the same hemisphere attached to its end. Deflection of the glass cantilever beam was measured with a laser scan micrometer (LS-3034; Keyence, Woodcliff Lake, NJ). The sensor assembly (actuator plus sensing element) was connected to a manual stage (462-XY; Newport, Irvine, CA) to position the hemisphere over the center of the microscope optics. The adhesive samples were placed on another manually controlled stage (562-XYZ; Newport, Irvine, CA) with the patterns facing toward the hemisphere. Custom real-time software controls the actuator to move the hemisphere into contact with the fiber sample at a fixed velocity until a pre-specified preload is reached. After pausing for a pre-specified period of contact time, the hemisphere is then retracted at a fixed velocity until it detaches from the sample. The software continually captures the deflection data from the laser micrometer as well as video from the microscope that is time-stamped for correlation with the force data. The load cell provides a force resolution of approximately 0.1 mN with a maximum deflection of 0.1 mm for a 25 g load (2414 N/m stiffness). The spring constant of the glass cantilever was measured to be 8.0 N/m which, when combined with the measurement precision of the laser micrometer, results in an overall force resolution of approximately 10 μ N for this system. During tests with oil-coated pillars, the hemisphere was cleaned using a lens paper and a lens cleaning fluid (Cat. #1767136; Kodak, Rochester, NY) before each measurement to remove any liquid from the previous test.

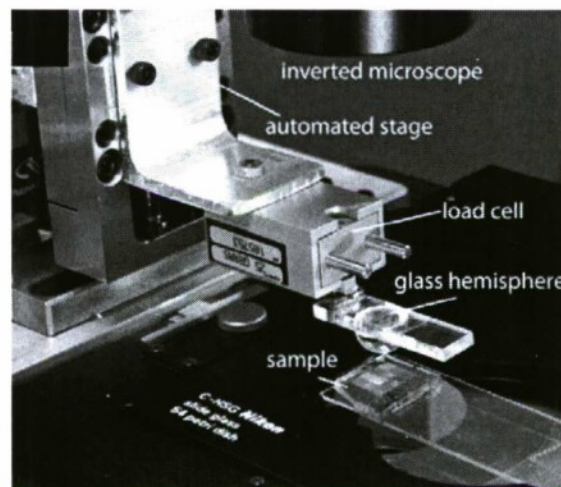


Figure 9. Adhesion characterization system set up for millinewton range measurements.

4.2 Flat-Flat Tensile Adhesion Measurement System

The major challenge in flat-flat measurement is alignment of the two contacting surfaces; this is accomplished using a simple passive alignment mechanism (Figure 10) An automated high precision linear actuator (MFA-CC, Newport) controls cantilever from which a ball/disk structure hangs by a compliant string. The fiber array to be tested is attached to the underside of the disk with the fibers facing down. Underneath this mechanism, the substrate is rigidly attached to a 10 lb load cell (MLP-10, Transducer Techniques), which is itself rigidly attached to the tabletop. When the cantilever is lowered and contact is made between the fiber sample and the substrate, the string goes slack allowing the sample and substrate to passively align through gravity. The cantilever is lowered further until it contacts the ball, pushing the two surfaces together. Custom real-time software controls the actuator at a fixed velocity until a pre-

specified preload force is reached. After pausing for a pre-specified amount of “contact time,” the sample is then retracted at a fixed velocity until it detaches from the substrate. The software continually captures the force data from the load cell.

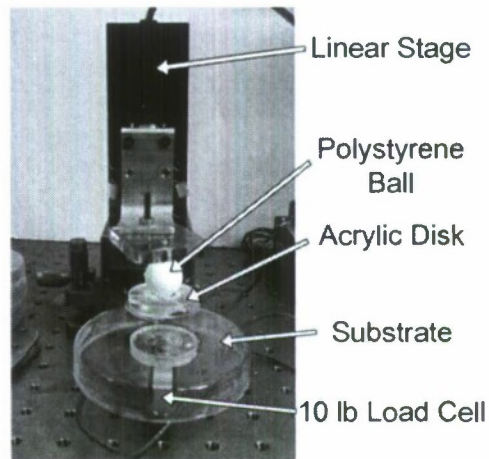


Figure 10. Tensile adhesion measurement setup with passive alignment mechanism.

4.3 Sealing Measurement System

To test the sealing performance of various samples, a simple vacuum-assisted setup was constructed (Figure 11). The sample, in the shape of an annulus, is attached to the end of a nozzle. This nozzle is connected by a flexible tube to a vacuum pressure gauge and syringe. The nozzle is fixed so that the sample faces upward. A substrate is then placed on top of the sample and loaded to specification. The plunger on the syringe is then pulled out to create a suction of 25 mm water column height (monitored with the pressure gauge). The time required for this suction to dissipate is measured. For the DOD required leakage rate of 15 mL/min for exhalation valves, the leakage time cannot be less than 36 s for this system.

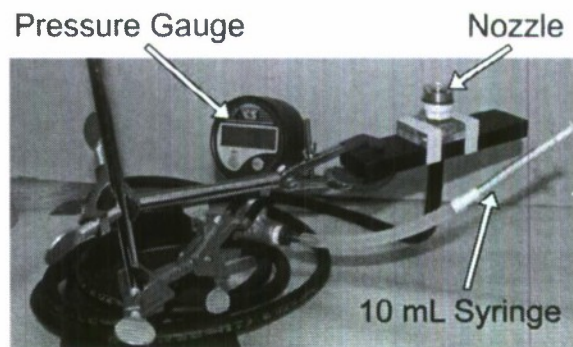


Figure 11. Sealing measurement setup.

5. MODEL VERIFICATION

5.1 Dry Adhesion

Experiments performed by Mike Murphy and Burak Aksak using the sphere-flat tensile adhesion measurement system with polyurethane microfibers (with and without spatulate tips) showed that the dry adhesion model provided a reasonable approximation of the pull-off force.^{19,27} Using fibers 20-25 μm in diameter of different heights and angles, the results of adhesion tests matched fairly well with simulations (see Figure 12). Similar tests were done with microfibers with spatulate tips, with the simulations effectively predicting adhesion performance.

5.2 Wet Adhesion

Again using the sphere-flat tensile adhesion measurement system, the PDMS micropillars with oil coating were tested with a 6 mm diameter glass hemisphere (QU-HS-6; ISP Optics, Irvington, NY). All measurements were for the adhesion of a single pillar. In most cases, there was only a single pillar in contact; when multiple-pillar contact occurs the central pillar detaches last and its adhesion peak can be isolated from the data.

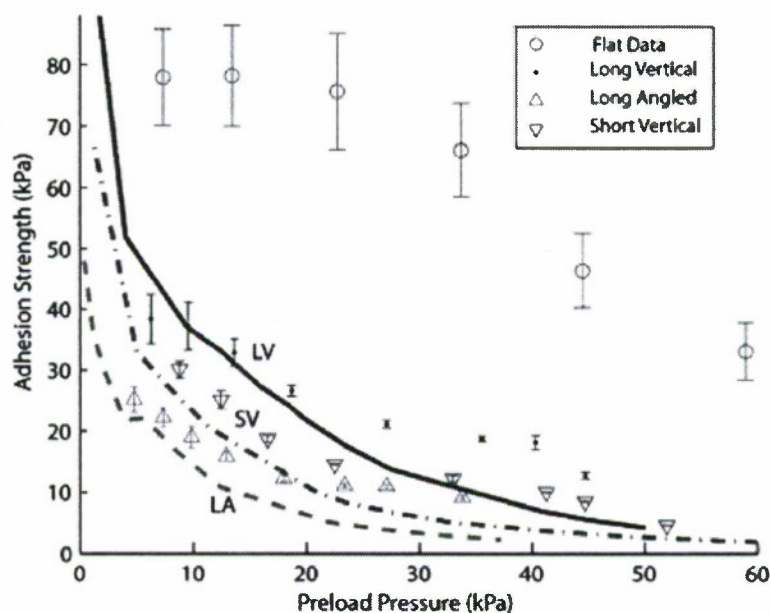


Figure 12. Adhesion strength as a function of preload pressure. [The simulation results are lines (LV, long vertical; LA, long angled; SV, short vertical), and the experimental data are markers (adapted from Aksak *et al.*)]¹⁹

A major factor in the capillary force model is the height of the liquid bridge, as the surface tension term increases with decreasing volume (related to the height) and the viscous term is inversely proportional to the height cubed. The easiest way to control the amount of liquid volume applied to the micropillars is to control the thickness of the spun liquid layer prior to stamping. As explained in Section 3.2, this is accomplished by diluting the pure silicone oil with a solvent that evaporates after spinning. Three solutions were prepared with 1, 4, and 10% silicone oil by weight. These solutions, along with pure silicone oil, were spun onto glass slides with the same spin parameters as specified in Section 3.2. The resulting thin films were

stamped onto 95 μm diameter pillars, and their adhesion was measured with 1 mN preload, 2 s contact time, and 5 $\mu\text{m/s}$ retraction speed. Figure 13 depicts the adhesion measurement results, clearly showing that decreased liquid volume, and, therefore, decreased liquid bridge height, results in higher adhesion. As a result, unless otherwise noted, the 4% silicone oil solution was used during liquid application to increase the measured adhesion forces. The 1% solution, though found to be superior in adhesion here, was not perfectly repeatable and thus not used.

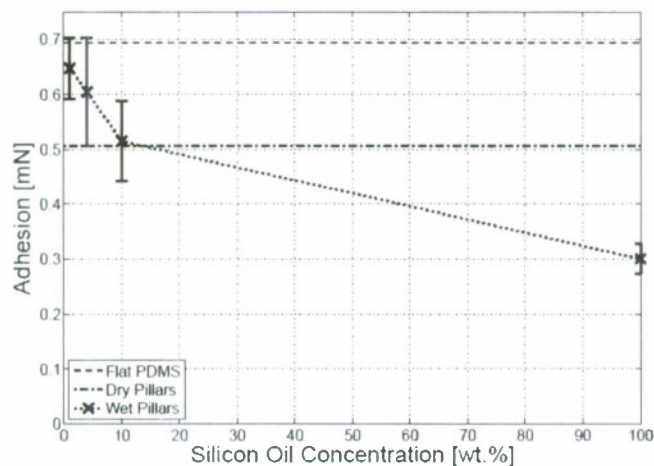


Figure 13. Adhesion experiment results as function of silicone oil concentration prior to spinning for 95 μm diameter, 125 μm tall, 71.3 μm edge-to-edge spacing pillars with 1 mN preload, 2 s contact time, and 5 $\mu\text{m/s}$ retraction speed on a 6 mm glass hemisphere. (Adhesion of flat PDMS and dry PDMS pillars with the same geometry are included for comparison.)

The diameter of the pillars was varied for the model comparison. These pattern diameter tests were performed with the retraction speed set to 5 $\mu\text{m/s}$, a 5 mN preload, and 2 s contact time. The micropatterns tested varied in diameter from 80 μm to 340 μm . Three measurements were taken for each diameter, and an effort was made to choose three cylinders with similar applied silicone oil volume. To obtain the plot of adhesion strength, the standard measure of adhesion performance, seen in Figure 14, the measured adhesion values are divided by the observed contact area of the single pillar tip.

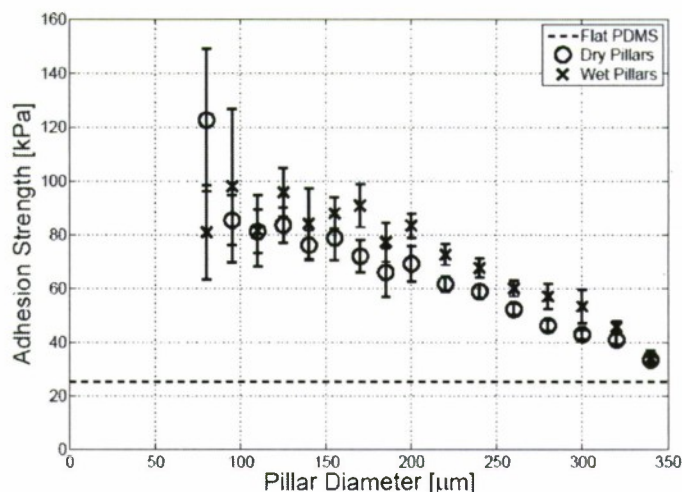


Figure 14. Adhesion strength experiment results as function of pillar diameter for 125 μm tall pillars with 5 mN preload, 2 s contact time, and 5 μm/s retraction speed on 6 mm glass hemisphere. Pillars were tested both dry and with liquid applied. (The adhesion strength of flat PDMS is included for comparison.)

Standard theory predicts increasing dry adhesion strength for smaller cylinders,²¹ and this is consistent with our tests. The pillars with a thin oil coating applied show approximately 25% enhanced adhesion over the dry pillars for diameters larger than 150 μm, but this drops off at smaller diameters. This plateau can be explained by the effect of the liquid application. If the estimated normalized volumes ($\hat{V} = V/r_p^3$, where V is the volume of liquid and r_p is the radius of the pillar) for the different diameter micropatterns are plotted (Figure 15), an effect of the chosen liquid application method becomes apparent; the smaller diameter micropatterns pick up a greater normalized volume.

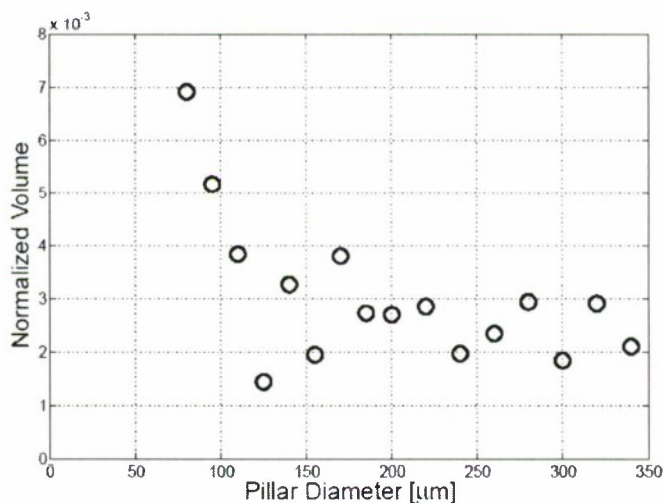


Figure 15. Estimated normalized volume as function of pillar diameter due to stamping method of liquid application. (These estimates are based on top-view optical microscope images taken just prior to testing.)

Using these experimental results, the proposed model can be validated. The only parameter in eq (13) that is not well defined is the initial height of the liquid film, h_0 . This value depends on the liquid application process as well as on the applied preload and contact time. Therefore, to determine the feasibility of the model, the h_0 values required to obtain the measured forces for the different diameter tests seen in Figure 14 were calculated. This was done by iterating the model simulation with differing h_0 values until the experimental force values were obtained. As seen in Figure 16, the results range from 1.1 to 3.2 μm ; although these initial film thicknesses result in volumes roughly 10 times greater than the optical estimates presented earlier, there are many uncertainties involved in the optical estimate and this deviation does not seem unreasonable. Indeed, the basic trend of the estimate (volume roughly inversely proportional to radius) is mirrored in the model calculations.

Taking these fitted h_0 values, the contributions of surface tension, pressure drop (related to the curvature of the liquid surface), and viscous effects (Stefan equation) can be extracted from the model (see Figure 16). The van der Waals force is also calculated, but is at least four orders of magnitude less than the surface tension force and is thus left off the graph and is assumed to be negligible. The surface tension component increases linearly with pillar diameter, but remains three orders of magnitude less than the viscous thin film contribution for the entire range and appears to be constant at zero in the figure. The pressure component increases as well but for pillars larger than 150 μm is significantly less than the viscous contribution. Thus, we see that for large pillars the viscous term is dominant in determining the adhesive performance. However, for pillars smaller than 150 μm , the pressure component approaches the same value as the viscous term.

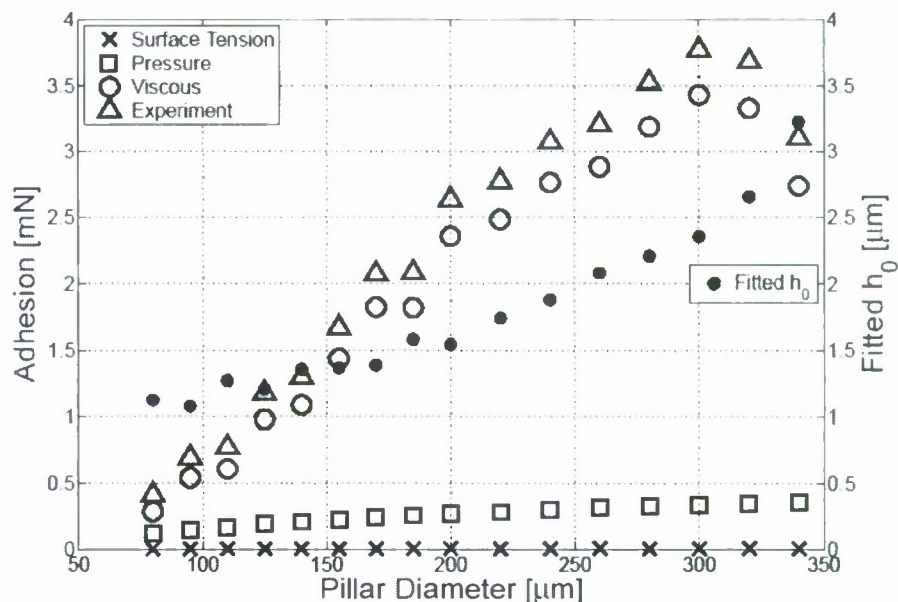


Figure 16. Fitted h_0 values used to match the model simulations with experimentally measured wet adhesion values. (Also shown are the surface tension, pressure, and viscous force contributions as calculated by the model.)

To further explore this trend, the model was used to calculate the four forces for pillars smaller than 80 μm in diameter. To mimic the effects of the liquid application procedure, the initial height h_0 of the liquid film was fixed at 0.75 μm and the liquid volume was calculated

as this h_0 multiplied by the area of the top of the pillar. This h_0 value was similar to the initial height for the $80\ \mu\text{m}$ pillars in the experiments as calculated in the previous paragraph. As seen in Figure 17, at large pillar diameters, the viscous term is dominant and the surface tension force is almost negligible in comparison. As the pillar diameter decreases, the viscous term decreases more rapidly than the other two terms, leading to the pressure component becoming the largest contributor at about $40\ \mu\text{m}$. Both of these decrease further with decreasing pillar diameter until the surface tension force becomes largest at $2\ \mu\text{m}$ (seen in the inset to Figure 17). The van der Waals force is negligible and left off the graph since it is at least five orders of magnitude less than the next smallest contributor. The trends in the three liquid forces can be easily explained with simple scaling arguments. The Stefan equation contains an R^4 term, the pressure component an R^2 term (surface area of pillar), and the surface tension component scales only linearly (circumference of pillar). This means that as the pillars get smaller, the viscous component diminishes faster than the pressure component. As the pillars get even smaller, these two components continue to shrink faster than the surface tension force, which eventually becomes dominant. If the value of h_0 is increased, the transition points move to the right (larger diameter pillars).

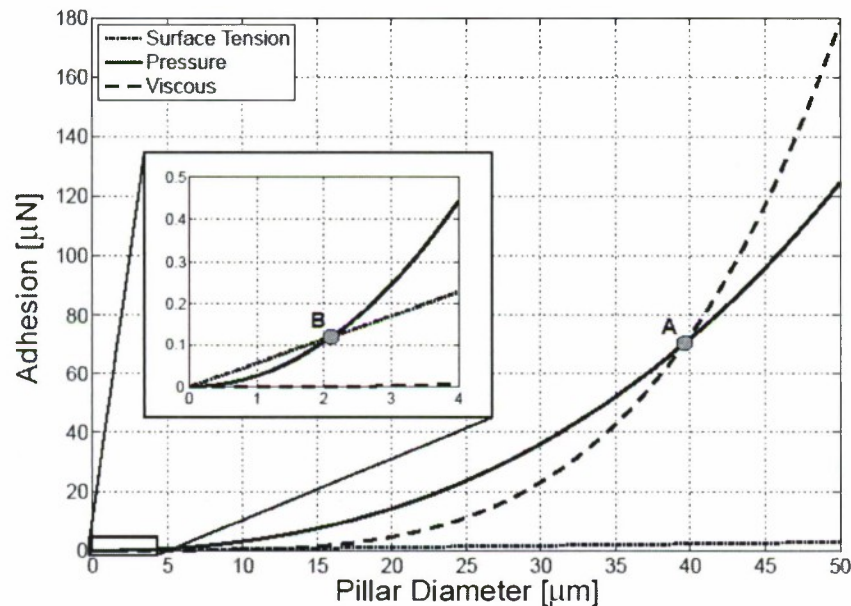


Figure 17. Model simulation with initial height h_0 held constant at $0.75\ \mu\text{m}$. (Point A identifies the transition between pressure dominated adhesion and viscous force dominated adhesion. Inset zooms in on point B, the transition between surface tension dominated adhesion and pressure dominated adhesion at $2\ \mu\text{m}$.)

It is interesting to note that the transition to surface tension dominated adhesion for the chosen h_0 takes place at $2\ \mu\text{m}$, the actual diameter of beetle fibers.² At this diameter, the viscous force is negligible, so it raises the question of why natural systems use viscous secretions at all. It would seem as though a less viscous substance would be less biologically taxing to produce, so animals would not bother using such viscous oils. Perhaps the assumption of constant initial height will not apply if comment is to be made on natural systems. An alternative assumption is to fix the normalized volume of liquid \hat{V} ; if the entire pillar scales down by a certain factor, the volume of liquid will also scale by the same factor. The results of this

simulation (with $\hat{V} = 0.06$ chosen to be similar to the calculated normalized volume for the 80 μm pillars) can be seen in Figure 18. Unlike the previous simulation, all three liquid forces scale linearly with pillar radius (the surface tension force is 500 times less than the viscous force and thus appears to be constant at zero in the figure). Assuming $\hat{V} \approx \pi h/R$, the viscous force eq (10) can be rewritten in terms of \hat{V} to show that this component now is proportional to only R . If $\Delta P(\hat{V})$ is a function of $1/R$, the pressure term is likewise a linear function of R . Decreasing the value of \hat{V} results in the increase of the slope of the viscous force line and the decreases of the slopes of the surface tension and pressure lines. The increase in the viscous force slope is much greater than the decreases in the other two slopes resulting in higher overall adhesion for smaller \hat{V} .

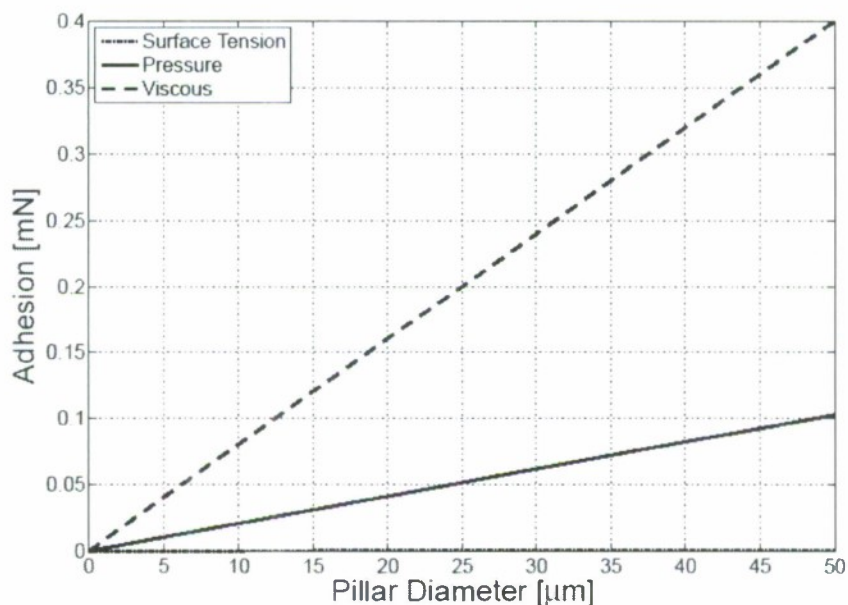


Figure 18. Model simulation with normalized volume \hat{V} held constant at 0.06. (The surface tension force is a linear function of pillar diameter, but is 500 times smaller than the viscous force and appears to be constant at zero.)

Because all the liquid force trends are linear, a plot of adhesion strength obtained by dividing the adhesion values by the area of each pillar (πR^2) would yield an inverse function of R . Therefore, a patch of densely packed small pillars would have higher adhesion than an equal area of densely packed larger pillars. However, there is a well known density limit where the pillars stick to one another known as lateral collapse²⁸ that must be taken into account when designing micropillar arrays. A final note must be made concerning the van der Waals force in this simulation. This force was again left off the graph since it is negligible for pillar diameters larger than 1 μm . However, the van der Waals force increases with smaller pillar diameter (approximately as an inverse function of R) and at very small pillar diameters (less than 1 μm), the magnitude of this force approaches that of the surface tension force. At even smaller diameters (less than 10 nm), the van der Waals force exceeds all of the liquid forces. At this length scale, though, the continuum mechanics used in the liquid force models is no longer valid and molecular dynamics is necessary to complete the analysis.

6. ADDITIONAL SPHERE-FLAT MEASUREMENTS

With the models shown to be sufficient, further measurements can be made to better understand the requirements for adhesion to human skin.

6.1 Wet Microfibers on Glass

The first step was combining the wet and dry adhesives by coating a sample of the polyurethane microfibers with oil using the same process described in Section 3.2. The chosen microfiber sample had a 30 μm diameter, 50 μm edge-to-edge spacing, and 120 μm tall vertical fibers. This diameter is near the resolution limit of printed transparency masks, and the less dense spacing allows for larger diameter spatulate tips and more interesting thin film effects. For both rigid and soft substrates, four different polyurethane samples were tested: flat ST-1060, unmodified microfibers (bare), microfibers with spatulate tips, and microfibers with attached thin film. Each of the three microfiber samples was also coated with a thin layer of silicone oil for a total of seven adhesive samples. The results shown are for the entire contact area comprising multiple fibers. In addition, it was no longer possible to identify and measure the pools of silicone oil on the fiber tips from optical microscope images as with the micropillars. The main evidence that there was silicone oil on the tips came from viewing the hemisphere after contact upon which the silicone oil is easily visible.

The adhesion results of the seven samples on a 6 mm glass hemisphere are shown in Figure 19. The adhesion enhancements reported from dry thin film²⁵ and dry spatulate tipped fibers¹⁹ have been successfully replicated. The dry microfibers with no tip modification also performed poorly, as expected. The wet microfibers with no tip modification show a decrease in adhesion from the dry, again as expected from the trend seen in Section 5.2 where the small diameter pillars pick up too much oil as a result of the liquid application process. Applying silicone oil to the thin film sample results in a marked decrease in adhesion. This is unsurprising as the spherical contacting surface allows the liquid spread over the continuous contact area to pool into one large bridge, greatly reducing the adhesion force. Most intriguing is the dramatic enhancement seen in the spatulate tipped microfibers coated with silicone oil, at times more than doubling the dry adhesion of spatulate tipped microfibers and tripling that of flat ST-1060 polyurethane. The exact mechanism for this enhancement remains a challenge for future work.

6.2 Soft Sphere

The next step towards understanding adhesion to human skin is changing the substrate to a soft material. Although the model includes the softness of the substrate in the effective Young's modulus K in eq (2), there could be additional unforeseen effects caused by the substrate deformation. F-15 polyurethane (BJB Enterprises, Tustin, CA) was chosen for its softness (Young's modulus of approximately 200 MPa), transparency, and non-tacky surface. The glass hemisphere used for the rigid surface tests was molded in pink silicone rubber (HS II; Dow Corning, Midland, MI) to create a negative. The polyurethane was then molded in the negative to create an exact replica of the 6 mm glass hemisphere.

PDMS micropillars

First, the simple PDMS micropillars were tested. These experiments investigated the effect of pillar diameter, preload, and retraction speed. As in the previous micropillar tests, all measurements were for the adhesion of a single pillar. In most cases, there was only a single

pillar in contact; when multiple-pillar contact occurs the central pillar detaches last and its adhesion peak can be isolated from the data.

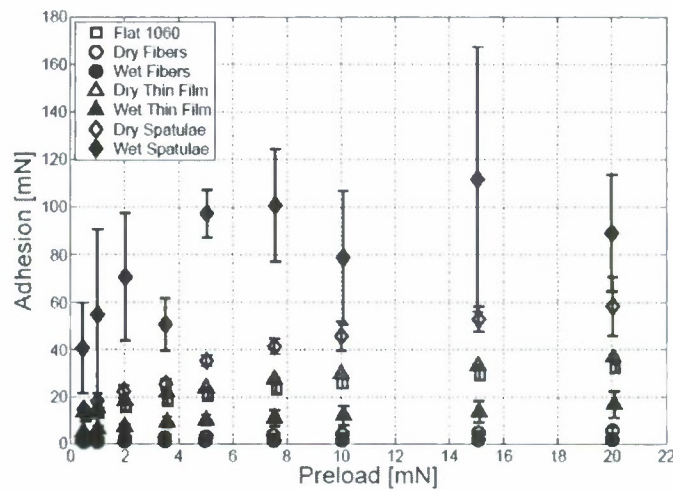


Figure 19. Adhesion strength experiment results as function of preload for 30 μm diameter, 50 μm edge-to-edge spacing, 125 μm tall polyurethane pillars with 2 s contact time and 5 $\mu\text{m}/\text{s}$ retraction speed on a 6 mm glass hemisphere.

Micropillar Diameter: As in the previous tests, the pattern diameter experiments were performed with the retraction speed set to 5 $\mu\text{m}/\text{s}$, a 5 mN preload, and 2 s contact time. The micropillars tested varied in diameter from 80 μm to 340 μm . Three measurements were taken for each diameter, and an effort was made to choose three pillars with similar applied silicone oil volume. The results, shown in Figure 20, show a similar trend to that seen for the smooth, rigid hemisphere (Figure 14). The volume of silicone oil on each pillar was again estimated using optical microscope images and the result was almost identical.

Preload: The preload experiments were conducted with 200 μm diameter micropillars and nine preloads varying from 0.5 to 20 mN, 2 s contact time, and 5 $\mu\text{m}/\text{s}$ retraction speed. Again, three measurements were taken for each preload, with an effort made to choose cylinders with similar applied silicone oil volume. The results are shown in Figure 21.

The measured adhesion strength reveals very little correlation with the applied preload. Typically, viscoelastic materials display a saturation curve when subjected to different preloads,²⁹ with soft materials saturating at lower preloads than more rigid ones. It is possible that the F-15 hemisphere has already hit its saturation point by 0.5 mN of preload.

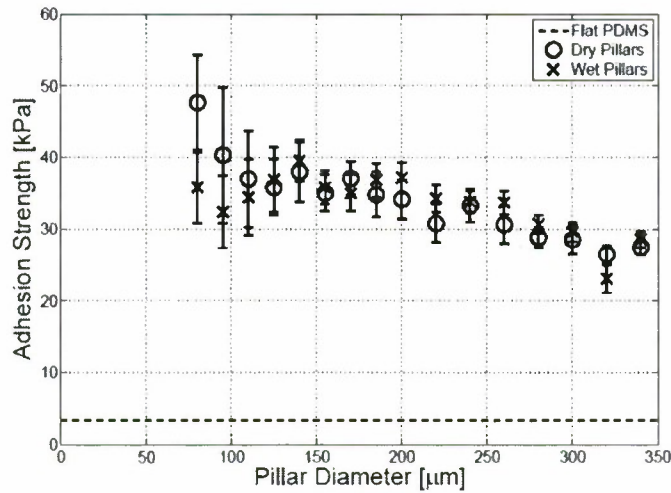


Figure 20. Adhesion strength experiment results as function of pillar diameter for 125 μm tall pillars with 5 mN preload, 2 s contact time, and 5 $\mu\text{m/s}$ retraction speed on 6 mm soft polyurethane hemisphere. (Pillars were tested both dry and with liquid applied. The adhesion strength of flat PDMS is included for comparison.)

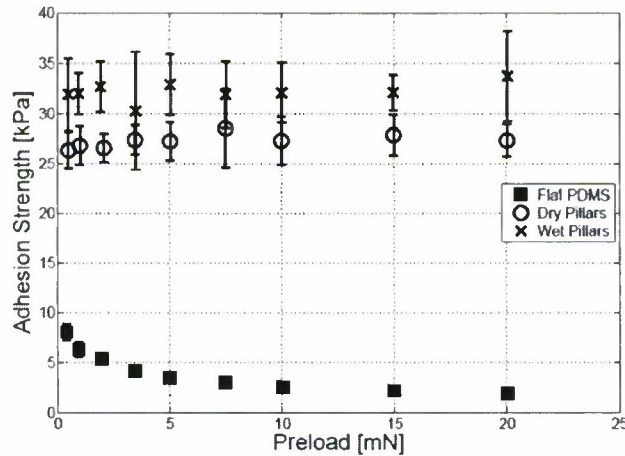


Figure 21. Adhesion strength experiment results as function of preload for 200 μm diameter, 125 μm tall pillars with 2 s contact time and 5 $\mu\text{m/s}$ retraction speed on a 6 mm soft polyurethane hemisphere. (Pillars were tested both dry and with liquid applied, and flat PDMS was tested for comparison.)

Retraction Speed: The speed tests were conducted with 200 μm diameter micropatterns, 5 mN preload, 2 s contact time, and thirteen retraction speeds varying from 1 $\mu\text{m/s}$ to 1 mm/s. Three measurements were taken for each retraction speed, with an effort made to choose cylinders with similar applied silicone oil volume. The results in Figure 22 show that increased retraction speed leads to increased adhesion strength up to a saturation point at about 100 $\mu\text{m/s}$.

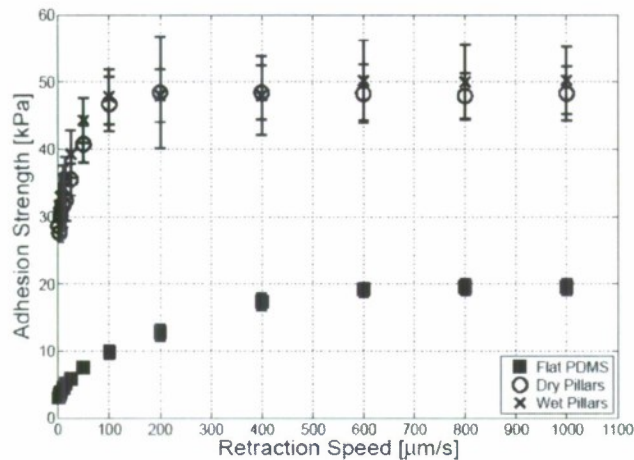


Figure 22. Adhesion strength experiment results as function of retraction speed for 200 μm diameter, 125 μm tall cylinders with 5 mN preload and 2 s contact time on a 6 mm soft polyurethane hemisphere. (Pillars were tested both dry and with liquid applied, and flat PDMS was tested for comparison.)

The experiments using a smooth, soft substrate show that adhesion to a soft substrate can still be approximated with the developed model. The only major difference between the rigid and soft smooth surfaces is the adhesive strength magnitude. For dry adhesion, this can be easily explained by noting that the combined effective Young's modulus K in eq (2) is significantly reduced, resulting in a corresponding reduction in the pull-off force in eq (1). In the case of wet adhesion, part of the reduction of adhesive force can be attributed to an increase in liquid film height, h_0 ; the deformation of the soft substrate dissipates some of the energy that would otherwise be used to squeeze the liquid. It is questionable whether this can explain the entire drop, however, so this result needs to be explored further.

Microfiber Tests

The adhesion results of the seven samples on a 6 mm soft polyurethane hemisphere are shown in Figure 23. As with the micropillars, the magnitudes of measured adhesion dropped significantly from rigid (Figure 19) to soft hemispheres. Unlike the micropillars, however, the deformation of the contacting surface seems to play a major role in the adhesion, at least for the silicone oil coated samples. The dry thin film and dry spatulate tipped microfibers show significant adhesive enhancement over the flat ST-1060 sample. The thin film sample is not as adversely affected by the silicone oil application as it was when using a glass hemisphere. Perhaps this is due to the F-15 deforming to become more like a flat surface, giving rise to thin film Stefan forces. An explanation for the drastically reduced adhesion seen when silicone oil is applied to the spatulate tipped microfibers has yet to be found, and remains a target of future work.

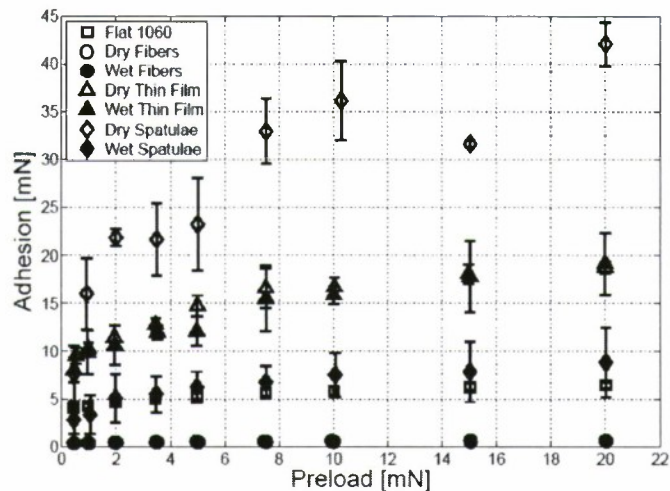


Figure 23. Adhesion strength experiment results as function of preload for 30 μm diameter, 50 μm edge-to-edge spacing, 125 μm tall polyurethane pillars with 2 s contact time and 5 $\mu\text{m}/\text{s}$ retraction speed on a 6 mm soft polyurethane hemisphere.

It was hypothesized that if the substrate is soft, the microfibers should be stiffer so as to increase the effective Young's modulus (eq 2). To test this, microfibers were made out of ST-1087 polyurethane which is about 2.4 times as stiff. These stiffer samples were then tested with both the glass and F-15 hemispheres. The measured adhesions showed the exact same trends as the ST-1060 microfibers, with the magnitude decreased by almost 40% on glass and almost 70% on F-15. Stiffer fibers do not appear to be the solution.

6.3 Rough, Rigid Surface

The next step towards understanding skin adhesion involves roughening the substrate. The models presented in Section 2 are purely for smooth substrates; rough surface adhesion modeling remains an ongoing challenge.

Although a decrease in the applied liquid volume has been shown to significantly aid capillary adhesion on smooth surfaces, an increase in the amount of liquid should also improve rough surface adaptation. It is hypothesized that beetles and other insects employ fibrillar structures (on the order of 2 μm in diameter)² to make up for the minute amounts of secreted liquid used (thickness on the order of 100 nm).¹ These fibrillar structures provide a level of compliance that enables intimate contact between a large number of the fiber tips and any micro/nanoscale rough surface with minimal preload. While not as thin as those seen in geckos that use dry adhesion, the loss of adaptability in the larger structures is made up for by the ability of the liquid to fill small-scale roughnesses.

To test this hypothesis, adhesion measurements were performed with a surface much rougher than the glass or F-15 hemispheres. Several surfaces were tried, but the most illustrative was found to be a 1/4" diameter, 3003 aluminum ball lightly sanded with fine grit sandpaper. Using an atomic force microscope, the surface roughness was measured to be 650 nm root-mean-square (RMS) (compared to 17.7 nm RMS for the glass hemisphere used in the smooth, rigid surface adhesion experiments). The 200 μm diameter PDMS micropatterns were tested with seven preloads varying from 1 to 50 mN, 2 s contact time, and 5 $\mu\text{m}/\text{s}$

retraction speed. In addition to the thin oil layer, a sample with an application of undiluted 10000 cSt oil was tested as well. The results, seen in Figure 24, show a dramatic adhesion enhancement for the thick oil layer. The added surface roughness drastically decreased the adhesion seen for the flat PDMS, dry pillars, and thin oil-coated pillars due to a reduction in contact area; the thicker oil coating could fill in the roughness resulting in a much lower loss of contact area, and therefore performs much better on this surface.

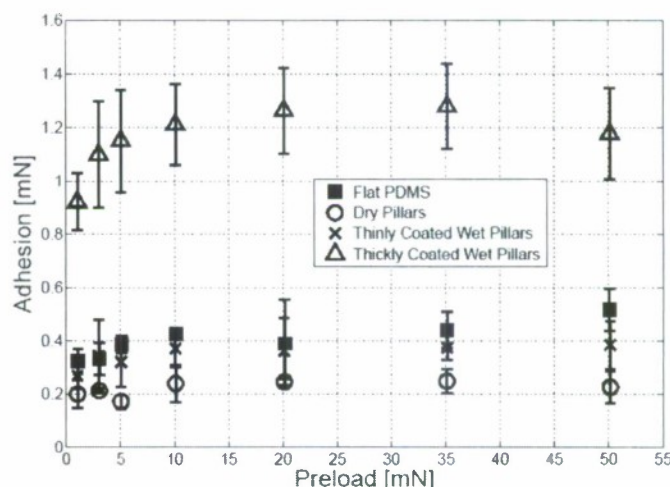


Figure 24. Adhesion experiment results as function of preload on sanded aluminum substrate for 200 μm diameter pillars, 2 s contact time, and 5 $\mu\text{m}/\text{s}$ retraction speed. (Three different pillar surface conditions were tested: dry with no liquid applied, a thin coating of 10000 cSt silicone oil, and a thick coating of 10000 cSt silicone oil. Adhesion of flat PDMS with the rough substrate is included for comparison.)

6.4 Summary

The experiments performed with the sphere-flat tensile adhesion measurement system showed the feasibility of the proposed fibrillar adhesives. These micro-scale tests demonstrated that a combination of microfibers and a thin oil coating was capable of a large adhesion enhancement on a rigid smooth surface. In addition, adhesion to a soft smooth surface was shown to be enhanced by microfibers, although a thin oil coating appeared to be detrimental. Finally, a thicker oil coating was found to be necessary for roughness adaptation when contacting a roughened rigid surface. The next step is to expand these small scale tests to larger areas to demonstrate a macro-scale ability to adhere to these differing substrates.

7. FLAT-FLAT TENSILE ADHESION TESTS

For the macro adhesion tests, all of the microfibers were fabricated to be 120 μm tall, perfectly vertical polyurethane fibers. The fiber diameters and densities (given in edge-to-edge spacing) are listed in Table 2 below. The densities will be referred to as low, medium, and high in the rest of this report. Note that the 30 μm fibers were only fabricated with low density, and the 100 and 50 μm fiber densities were only medium and high. Each geometry was made both bare and with spatulate tips.

Table 2. Sample geometry for experimentally tested polyurethane fibers. (Each fiber diameter was fabricated with the fiber spacing given below it.)

Diameter (μm)	100	80	50	40	30
Fiber Spacing (μm)	140, 60	160, 100, 40	110, 70, 30	80, 50	50

7.1 Initial Tests on Glass

A series of adhesion tests on a flat rigid glass surface were performed to investigate the effects of four variables: pattern density (fiber spacing), fiber diameter, tip structure, and preload. Each sample was cut into an annulus shape (1 in. outer diameter, 1/4 in. diameter inner diameter) using a steel punch with an eye towards later sealing tests. These samples were tested on a glass Petri dish with preloads up to 5 N. Each data point corresponds to an average of three independent measurements. The results are summed up in Figure 25 with the data split into bare fiber results and spatulate tipped fiber results.

In all cases, increasing preload results in increased adhesion. Although not predicted in the simplified model, some preload dependence is expected due to the viscoelasticity of the polymer. In addition, the glass surface and fiber tips are not perfectly smooth, so higher preload results in greater surface contact.

As indicated in eq (6), for a perfectly smooth surface, the adhesion should increase with larger diameter. This is not seen in the results. For the bare fibers (Figure 25a), this is likely due to the roughness of the glass surface and fiber tips. For the spatulate tipped fibers (Figure 25b), the geometry of the tips is also a factor.

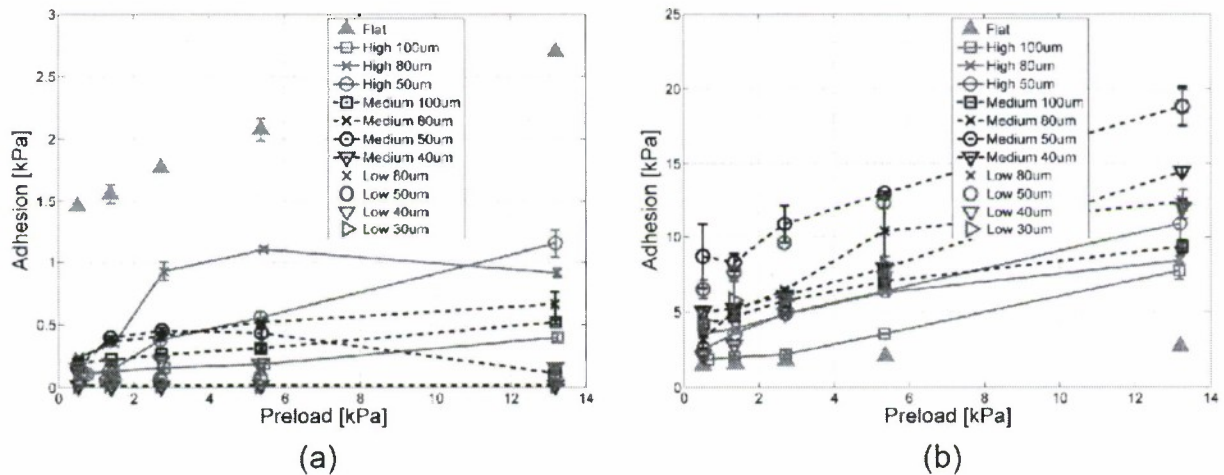


Figure 25. Plot of adhesion results vs. preload for (a) bare and (b) spatulate-tipped fiber arrays on flat glass substrate. [Data are grouped by fiber density (line style) and fiber diameter (marker).]

Since the pattern density dictates the number of fibers in the array, one would expect denser fibers to have higher adhesion. This is seen in the bare fibers, but not the fibers with spatulate tips. An in-depth discussion follows in the tip structure analysis.

Clearly, the fibers with spatulate tips show much better adhesion than fibers without tips. Every tipped fiber sample demonstrated greater adhesion than the flat control, while every bare fiber sample was well below the flat control. The samples that exhibited the highest adhesion were 50 μm diameter, low and medium density. At the highest preload, these samples showed almost 7 times as much adhesion as the flat sample. To determine why the low and medium density arrays performed significantly better than the high density fibers, images were taken of the spatulate tips on 50 μm fibers with an optical microscope (Figure 26). These images showed that the diameter of the spatulate tip varied greatly. The space restrictions in the high density array limited the flat tip to be barely larger than the fiber itself (65 μm), whereas the medium and low density fibers showed tip diameters of 105 and 120 μm , respectively. An area fraction calculation showed 54%, 64%, and 45% coverage for low, medium, and high density arrays. The diameter effect can be seen more clearly here; the much larger tips result in greater adhesion. Despite the lower area coverage in the low density array, the increased tip diameter more than compensates for the lost adhesion.

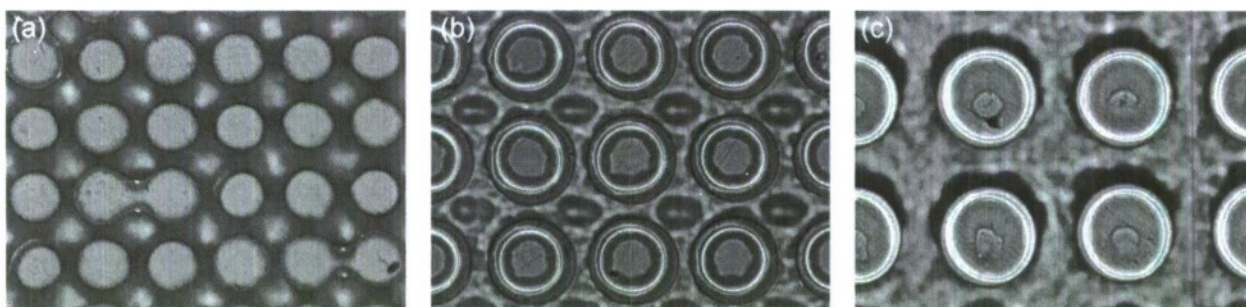


Figure 26. Top view optical microscope images of 50 μm diameter fibers with spatulate tips; (a) high density, (b) medium density, and (c) low density. (The three images are at equal magnification, showing difference in tip diameter.)

7.2 Pig Skin Tests

A feasibility test on pig skin was conducted using the two best fiber geometries from the rigid glass tests as well as a flat control and a bare fiber sample for comparison. A sample of pig skin was obtained from the local meat market to use as a biological facsimile for human skin. The results from this experiment (Figure 27) were markedly different from the rigid substrate results. The only similarity is the preload dependence. All of the fiber samples, regardless of tip structure and density, tested below the flat control, which in itself was well below the adhesion value measured for the rigid glass substrate. Clearly, the rougher, compliant substrate presents much more difficulty in developing a robust adhesive.

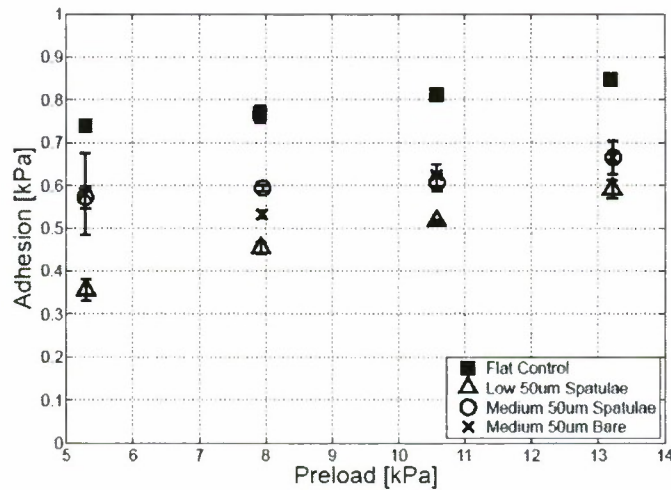


Figure 27. Plot of adhesion results vs. preload for various fiber arrays on flat pig skin.

7.3 Reworked Glass Tests

Observations made during the large area measurements indicated that contact was not achieved across the entire 1 in. diameter sample. To get a more accurate measure of adhesion strength, the samples were cut down to ½-in. squares and retested on a glass slide that is smoother than the Petri dish. Based on the previous data that showed the best performance for medium density fibers with spatulate tips, only these were tested. In addition, two oil coatings were applied to the fibers for comparison: the thin oil coating used in the wet adhesion model verification; and a thick oil coating (no dilution prior to spinning). These tests were performed with a retraction speed of 100 μm/s, a 200 mN preload, and 5 s contact time. The results seen in Figure 28 show similar results from the previous tests, with the 50 μm fibers performing best. An enhancement of almost 100% for the thin oil coating for most of the fibers was a pleasant surprise.

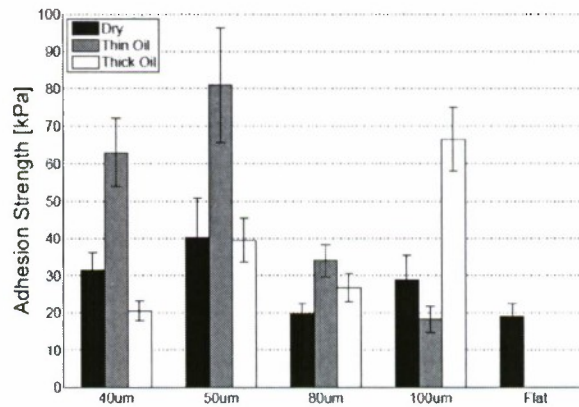


Figure 28. Flat-flat adhesion test results for medium spacing fibers with spatulate tips on glass.

7.4 Synthetic Soft Surfaces

The previous tests on pig skin revealed that there are a lot of potential variables that could be causing the measured decreased adhesion (skin oils, hair follicles, and surface roughness to name a few). To approach these problems more systematically, synthetic soft flat surfaces were fabricated out of the soft F-15 polyurethane.

Smooth F-15

The control experiment used smooth F-15 created by curing the polyurethane against a sheet of acrylic. The same samples used in the previous flat glass tests were used with the same test parameters (100 $\mu\text{m/s}$, 200 mN preload, and 5 s contact time). The results seen in Figure 29 are encouraging in that the decrease in adhesion from the glass substrate is not seen. While the thin oil coating does not decrease the adhesion as in the sphere-flat measurements, it does not produce nearly the same enhancement seen on glass. Maximum adhesion is observed with the same diameter fibers (50 μm) as in the previous tests.

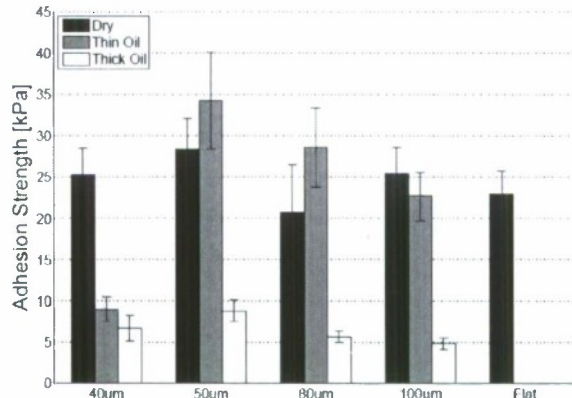


Figure 29. Flat-flat adhesion test results for medium spacing fibers with spatulate tips on smooth and soft F-15.

Textured F-15

Next, a textured F-15 surface was created by molding an aluminum plate. The aluminum was roughened by sandblasting to obtain an RMS roughness of 1.39 μm . A negative mold was created using pink rubber, and F-15 was then cured in the mold to create a soft polyurethane duplicate of the textured aluminum surface. Again, the same samples were tested with the same test parameters to obtain the results seen in Figure 30. As expected, there is decreased adhesion due to the F-15 surface texture. The best dry adhesion is seen in the smallest diameter (40 μm) fibers while the best overall adhesion is seen in the 50 μm diameter pillars with a thin oil coating. This wet adhesion is 25% better than the best dry adhesion.

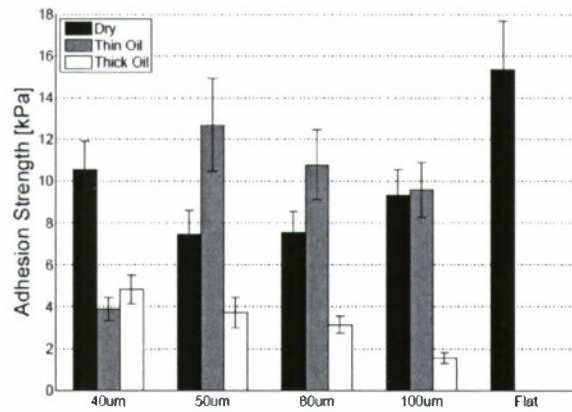


Figure 30. Flat-flat adhesion test results for medium spacing fibers with spatulate tips on textured soft F-15 with RMS roughness of 1.39 μm .

7.5 Wet Substrates

To mimic a sweat layer on the face, adhesion tests were performed with a thin water layer on the substrate. Unfortunately, the F-15 polyurethane is hydrophobic, precluding its use in these tests without some form of surface treatment. As a first test, a glass slide was used. The same samples used in the previous flat glass tests were used with the same test parameters (100 $\mu\text{m/s}$, 200 mN preload, and 5 s contact time) to obtain the results seen in Figure 31.

When compared with the previous tests, there is a definite decrease in adhesion when water is covering the surface. However, it can be seen that the fibrillar adhesives were more successful at maintaining some part of their adhesion than the flat control.

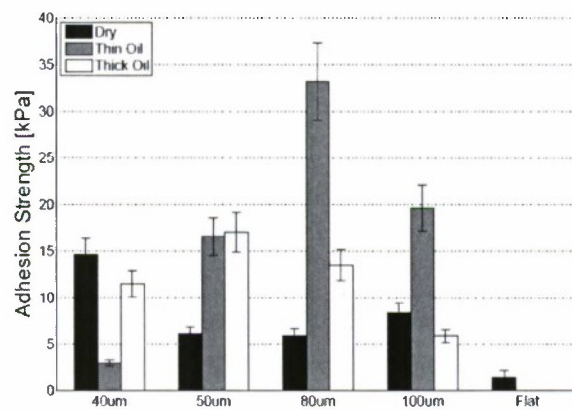


Figure 31. Flat-flat adhesion test results for medium spacing fibers with spatulate tips on glass with thin water layer.

7.6 Summary

The preliminary pig skin tests showed that adhesion to biological substrates remains a significant challenge. However, significant progress has been made in developing an adhesive to accomplish this goal. Adhesion to soft, textured surfaces as well as wet, rigid surfaces was demonstrated. The results suggest that the smallest diameter fibers are better suited for the purposes of adhesion to skin. In addition, while a promising area of future research, the addition of a thin oil layer does not enhance adhesion by a significant amount. When other concerns (including fabrication/reusability and oily residue) are taken into consideration, we conclude that a dry adhesive is the best option.

8. SEALING TEST RESULTS AND DISCUSSION

The most important quality that must be demonstrated is the ability to maintain a proper seal. Every sample listed in Table 2 (in Section 7) was tested on four surfaces with preloads up to 5.5 N. The four chosen surfaces included two rigid substrates (polystyrene and glass), one synthetic soft substrate (2.5 mm thick PDMS), and one biological substrate (pig skin). Tests with a flat polyurethane sample confirmed perfect sealing with little preload on all synthetic substrates, demonstrating that the sealing setup performs correctly. A preload of 1.5 N was required to meet the DoD leakage requirement on pig skin. In contrast, only one of the fibrillar adhesives demonstrated adequate sealing performance; 30 μm diameter fibers with a preload of 5.5 N showed a leakage rate of 7 mL/min. It is clear from these results that the fibrillar adhesives on their own are incapable of providing adequate sealing capabilities. By definition they have gaps that allow gases to pass through. However, if the fiber arrays are coupled with sealing structures with no gaps, a sealing material with the enhanced adhesion provided by the fibers can be accomplished.

Encapsulation

As a proof of concept, a simple procedure to encapsulate the fibers with a ring of solid polymer was used to demonstrate sealing with a fiber array. A fiber sample, already cut into the annulus shape, is placed fiber tips down on a flat surface. Uncured polyurethane in a viscous liquid state is poured around the edges and another flat surface and small weight are placed on top to maintain the sample's thickness. The liquid polymer penetrates the fiber array a short distance before curing. When cured, the sample is re-cut with the steel punch, resulting in a fiber array with an outer ring of solid polyurethane (Figure 32). In the future, such encapsulation structures can be included in the transparency mask used in the fabrication of the master template.

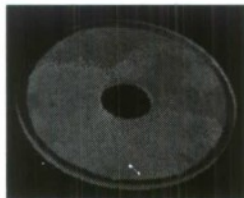


Figure 32. ST-1060 polyurethane molded fiber array, cut into 1 in. diameter annulus, with spatulate tips and encapsulation. (The fibers are 100 μm in diameter with 60 μm edge-to-edge spacing.)

Tests performed with encapsulated fibers showed no appreciable loss in adhesion due to the encapsulation procedure and structures. In addition, the sealing capability vastly improved, almost to the level of the flat control on all substrates. Integration of sealing structures similar to the one demonstrated here into the adhesive fabrication process is straightforward, and should result in a fibrillar adhesive that meets or exceeds the required DoD specifications for exhalation valve seal testing.

9. INITIAL FRICTION TESTS

One aspect of the synthetic fibrillar adhesive performance that has been overlooked thus far is friction. Although it is possible to maintain a good seal during slipping, it is desirable to prevent such shear motions as it becomes more likely for the seal to fail under these conditions. While outside the scope of the current work, preliminary friction measurements were performed on the textured F-15 polyurethane surface (1.39 μm RMS roughness). Although a thin layer of water could not be spread on the polyurethane, some measurements were taken with the entire surface immersed in water for some ballpark numbers. 30 μm diameter microfibers with spatulate tips and no oil coating were used for these initial friction tests.

The friction measurement setup consists of a carriage that is connected by a string to the load point of a 10 pound load cell which is attached to a motorized stage. The adhesive sample ($\frac{1}{2}$ " x $\frac{1}{2}$ " square) is affixed to the underside of the carriage and placed on top of the substrate. If desired, weights can be placed in the carriage to increase the preload on the sample. The motorized stage pulls the carriage (and attached sample) across the substrate, while the load cell records the friction force.

The results of the friction tests using a flat ST-1060 control and the microfiber sample are given in Table 3 below. Clearly, the microfibers result in less friction than the flat control. They appear to perform slightly better than the flat sample under high preload in wet conditions, but these preliminary data are not sufficient to draw any hard conclusions.

Table 3. Friction measurements on soft F-15 polyurethane with 1.39 μm RMS roughness with pulling speed of 0.1 mm/s

Preload (N)	Substrate Condition	Flat ST-1060 Friction (N)	30 μm Microfibers Friction (N)
0.06	Dry	0.53 \pm 0.15	0.12 \pm 0.02
	Wet	0.13 \pm 0.02	0.08 \pm 0.01
0.55	Dry	1.26 \pm 0.16	0.60 \pm 0.07
	Wet	1.17 \pm 0.02	0.68 \pm 0.01

Much progress has been made toward the use of biologically inspired microfibrillar arrays for the improvement of mask sealing performance. Approximate models of dry and wet adhesion on smooth surfaces have been developed and experimentally verified. Fabricated synthetic adhesives with spatulate tips have demonstrated pronounced adhesion enhancements on smooth substrates (both rigid and soft). Adhesion tests on textured soft synthetic surfaces suggest minimization of the microfiber diameter to optimize adhesion. Furthermore, the addition of a thin oil layer was found to enhance adhesion only slightly, and the added complications that come with this option have led to the decision to concentrate on dry adhesives. Experiments conducted on a wet substrate showed that fibrillar surface is capable of adhering in these conditions, unlike a flat polymer surface. However, this adhesion is markedly decreased, suggesting that the synthetic adhesive must be over-designed on dry surfaces in order to maintain good performance in wet conditions. Sealing tests revealed that the microfibers on their own are incapable of maintaining a seal, but the simple addition of a sealing structure results in a capable sealant. Further research is required to optimize adhesion on rough, soft, wet substrates (akin to human skin).

Blank

LITERATURE CITED

1. Federle, W.; Riehle, M.; Curtis, A. S. G.; Full, R. J. An integrative study of insect adhesion: mechanics and wet adhesion of pretarsal pads in ants. *Integr. Comp. Biol.* 2002, 42 (6), 1100-1106.
2. Eisner, T.; Aneshansley, D. Defense by foot adhesion in a beetle (*Hemisphaerota cyanea*). *Proc. Nat. Acad. Soc. U.S.A.* 2000, 97 (12), 6568-6573.
3. Walker, G. Adhesion to smooth surfaces by insects - a review. *Int. J. Adhes. Adhes.* 1992, 13 (1), 3-7.
4. Lees, A. D.; Hardie, J. The organs of adhesion in the aphid *Megoura viciae*. *J. Exp. Biol.* 1988, 136, 209-228.
5. Stork, N. E. Experimental analysis of adhesion of *Chrysolina polita* (*Chrysomelidae: coleoptera*) on a variety of surfaces. *J. Exp. Biol.* 1980, 88, 91-107.
6. Dixon, A. F. G.; Croghan, P. C.; Gowing, R. P. The mechanism by which aphids adhere to smooth surfaces. *J. Exp. Biol.* 1990, 152, 243-253.
7. Autumn, K.; Liang, Y. A.; Hsieh, S. T.; Zesch, W.; Chan, W. P.; Kenny, T. W.; Fearing, R.; Full, R. J. Adhesive force of a single gecko foot-hair. *Nature* 2000, 405, 681-685.
8. Jagota, A.; Bennison, S. J. Mechanics of adhesion through a fibrillar microstructure. *Integr. Comp. Biol.* 2002, 42, 1140-1145.
9. Arzt, E.; Gorb, S.; Spolaneck, R. From micro to nano contacts in biological attachment devices. *Proc. Nat. Acad. Soc. U.S.A.* 2003, 100 (19), 10603-10606.
10. Crosby, A. J.; Hageman, M.; Duncan, A. Controlling Polymer Adhesion with 'Pancakes.' *Langmuir* 2005, 21 (25), 11738-11743.
11. Hui, C. Y.; Glassmaker, N. J.; Tang, T.; Jagota, A. Design of biomimetic fibrillar interfaces: 2. Mechanics of enhanced adhesion. *J. R. Soc. Interface* 2004, 1 (1), 35-48.
12. Gorb, S. N. The design of the fly adhesive pad: distal tenent setae are adapted to the delivery of an adhesive secretion. *Proc. R. Soc. London, Ser. B* 1998, 265 (1398), 747-752.
13. Jiao, Y.; Gorb, S.; Scherge, M. Adhesion measured on the attachment pads of *Tettigonia viridissima* (*Orthoptera, insecta*). *J. Exp. Biol.* 2000, 203 (12), 1887-1895.
14. Wigglesworth, V. B. How does a fly cling to the under surface of a glass sheet? *J. Exp. Biol.* 1987, 129, 373-376.
15. Gillett, J. D.; Wigglesworth, V. B. The climbing organ of an insect, *Rhodnius prolixus* (*Hemiptera; reduviidae*). *Proc. R. Soc. London, Ser. B* 1932, 111 (772), 364-376.

16. Votsch, W.; Nicholson, G.; Muller, R.; Stierhof, Y. D.; Gorb, S.; Schwarz, U. Chemical composition of the attachment pad secretion of the locust *Locusta migratoria*. *Insect Biochem. Mol. Biol.* 2002, 32 (12), 1605-1613.
17. Kosaki, A.; Yamaoka, R. Chemical composition of footprints and cuticula lipids of three species of lady beetles. *Jpn. J. Appl. Entomol. Zool.* 1996, 40 (1), 47-53.
18. Qian, J.; Gao, H. Scaling effects of wet adhesion in biological attachment systems. *Acta Biomater.* 2006, 2, 51-58.
19. Aksak, B.; Murphy, M. P.; Sitti, M. Adhesion of Biologically Inspired Vertical and Angled Polymer Microfiber Arrays. *Langmuir* 2007, 23, 3322-3332.
20. Maugis, D. *Contact, Adhesion and Rupture of Elastic Solids*; Springer: New York, 2000.
21. Spolenak, R.; Gorb, S.; Gao, H.; Arzt, E. Effects of contact shape on the scaling of biological attachments. *Proc. R. Soc. London, Ser. A* 2005, 462 (2054), 305-319.
22. Maugis, D. Adhesion of spheres: the JKR-DMT transition using a dugdale model. *J. Colloid Interface Sci.* 1992, 150, 243-269.
23. Bird, R. B.; Armstrong, R. C.; Hassager, O. *Dynamics of Polymeric Liquids, Volume 1, Fluid Mechanics*; John Wiley & Sons: New York, 1977.
24. Israelachvili, J. *Intermolecular & Surface Forces*; Academic Press: San Diego, CA, 1992.
25. Glassmaker, N. J.; Jagota, A.; Hui, C. Y.; Noderer, W. L.; Chaudhury, M. K. Biologically inspired crack trapping for enhanced adhesion. *Proc. Nat. Acad. Sci. U.S.A.* 2007, 104 (26), 10786-10791.
26. Xia, Y.; Whitesides, G. M. *Soft Lithography*. *Angew. Chem. Int. Ed.* 1998, 37 (5), 550-575.
27. Murphy, M.; Aksak, B.; Sitti, M. Adhesion and anisotropic friction enhancements of angled heterogeneous micro-fiber arrays with spherical and spatula tips. *J. Adhes. Sci. Technol.* 2007, 21 (12), 1281-1296.
28. Geim, A. K.; Dubonos, S. V.; Grigorieva, I. V.; Novoselov, K. S.; Zhukov, A. A.; Shapova, S. Y. Microfabricated adhesive mimicking gecko foot-hair. *Nat. Mater.* 2003, 2, 461-463.
29. Haiat, G.; Phan Huy, M. C.; Barthel, E. The adhesive contact of viscoelastic spheres. *J. Mech. Phys. Solids* 2003, 51, 69-99.